ÇUKUROVA UNIVERSITY
INSTITUTE OF NATURAL AND APPLIED SCIENCES

PhD THESIS

Khalil DADASHİ

OPTICAL PROPERTIES OF INHOMOGENEOUS MICRORESONATORS

DEPARTMENT OF PHYSICS

ADANA-2017

ÇUKUROVA UNIVERSITY
INSTITUTE OF NATURAL AND APPLIED SCIENCES

OPTICAL PROPERTIES OF INHOMOGENEOUS MICRORESONATORS

Khalil Dadashi

PhD THESIS

DEPARTMENT OF PHYSİCS

We certify that the thesis titled above was reviewed and approved for the award of degree of the Doctor of Philosophy by the board of jury on 15/12/2017.

…….....	…….....	…….....
Prof. Dr. Ramazan ESEN	Prof. Dr. Hamide KAVAK	Prof. Dr. Emirullah MEHMETOV
SUPERVISOR	MEMBER	MEMBER
…….....	……	
Prof. Dr. Zeki YARAR	Asst. Prof. Dr. Mirbek TURDUEV	
MEMBER	MEMBER	

This PhD Thesis is written at the Department of Institute of Natural And Applied Sciences of Çukurova University.
Registration Number:

Prof. Dr. Mustafa GÖK
Director
Institute of Natural and Applied Sciences

ABSTRACT

PhD THESIS

OPTICAL PROPERTIES OF INHOMOGENEOUS MICRORESONATORS

Khalil Dadashi

ÇUKUROVA UNIVERSITY
INSTITUTE OF NATURAL AND APPLIED SCIENCES
DEPARTMENT OF PHYSICS

Supervisor : Prof. Dr. Ramazan ESEN
II. Supervisor : Prof. Dr. Hamza KURT
Year: 2017, Pages: 101
Jury : Prof. Dr. Ramazan ESEN
: Prof. Dr. Hamide KAVAK
: Prof. Dr. Emirullah MEHMETOV
: Prof. Dr. Zeki YARAR
: Asst. Prof. Dr. Mirbek Turduev

It is known that the spectra of optical modes supported by microresonators are shape and size dependent. We have introduced an additional parameter, i.e., spatially varying refractive index to tailor the spectra of optical modes in microdisc resonator while keeping size and shape intact. So, a new class of whispering gallery mode (WGM) microresonators, referred to as graded index (GRIN) microresonators, is proposed. On the other hand, the WGMs in optical microresonator resemble to the confined electron states in atoms. We have studied these new proposed structures as photonic atoms. A cluster of such microresonators can be named photonic mulecule. Then, the PT-symmetry condition has been studied in microresonators. In optics, the PT-symmetry condition translated to the complex refractive index. We have studied a new type of add-drop microring resonator made of gain and loss materials as a simple implementation of PT-symmetry in microphotonics. The modal analysis of the structure is investigated numerically. It is expected that the findings of GRIN microresonator may open up new research and device opportunities in photonics.

Key Words: Microresonators, Graded inedx, Maxwel's fish eye, Whispering gallery modes, Photonic atom, PT-symmetry,

ÖZ

DOKTORA TEZİ

HOMOJEN OLMAYAN MİKROREZONATÖRLERİN OPTİK ÖZELLİKLERİ

Khalil DADASHI

ÇUKUROVA ÜNİVERSİTESİ
FEN BİLİMLERİ ENSTİTÜSÜ
FİZİK ANABİLİM DALI

Danışman : Prof. Dr. Ramazan ESEN
II. Danışman : Prof. Dr. Hamza KURT
Yıl: 2017, Sayfa: 101
Jüri : Prof. Dr. Ramazan ESEN
: Prof. Dr. Hamide KAVAK
: Prof. Dr. Emirullah MEHMETOV
: Prof. Dr. Zeki YARAR
: Yrd. Doç. Dr. Mirbek TURDUEV

Bilindiği üzere, mikrorezonatör yapılarda uyarılan optik modların spektrumları, yapının boyutlarına ve şekline bağlıdır. Biz bu çalışmada ek bir parametre olarak; mikrodisk rezonatörde etkin kırılma indisinin konumsal değişimi tanımladık. Derecelendirilmiş kırıcılık indisli mikrorezonatörler, whispering gallery modes (WGM) rezonatörler içinde yeni bir sınıf olarak sunulmaktadır. Bu tip yapılarda elde edilen optik modların hapsedilmiş elektron durumlarına benzer özellikler göstermesi sebebiyle, bu tip yapılar fotonik atom olarak isimlendirilmektedir. Fotonik atomlardan oluşan zincir yapısına fotonik molekül denmektedir. Ayrıca, PT- simetri koşulları mikrorezonatör yapılarında incelenmiş olup halkalı yapının kompleks kırıcılık indisine sahip olduğu varsayılmıştır: Mikrorezonatör yapısının halkalı kısmının periyodik kazançlı ve kayıplı ortamlardan oluştuğu varsayılmış olup bu tipteki PT- simetrili rezonatör yapısının modal analizi nümerik olarak incelenmiştir. GRIN mikrorezonatörden elde edilen bu bulguları, fotonik alanında yeni araştırma ve uygulama fırsatları doğuracağı ümit edilmektedir.

Anahtar Kelimeler: Mikrorezonatör, Derecelendirilmiş kırılma indis, Fotonik atom, PT- simetri, Maxwell’s fish eye, Whispering gallery modes,

EXTENDED ABSTRACT

As the photonic devices, dielectric microspheres and similar geometries are optical elements that have attracted increased attention in recent literature due to their ability to exhibit on-resonance and off-resonance properties. It means that, in on-resonance case, they can select narrow part of the incident beam for further manipulation and processing. If we illuminate the circular structure laterally, its natural oscillations appear. These optical oscillations are known as whispering gallery modes (WGMs). On the other hand, in off-resonance case, which the circular structure is illuminated perpendicularly, photonic jets (PJs) appear in the shadow side. In this case, the light is squeezed and its intensity enhances.

WGM resonators have variety of applications in optical systems, such as optical filters, modulators, and sensors including biological sensors. One of the key performance metrics of an optical resonator is its quality factor (Q-factor), a measure of how much energy is stored in the resonator with respect to the energy lost per resonance cycle. This work studies a new method for achieving high optical Q-factor on spherical dielectric microresonators. We expect the graded index (GRIN) approach can increase the Q-factor in comparison with typical conventional microresonators.

GRIN structures have been widely studied in recent years, from invisibility cloaks and illusion devices, to planar lenses, such as Maxwell's fish eye (MFE). Fabrication of such structures, where the dielectric medium is modified rapidly on a few-wavelength scale, is challenging and limited by scattering loses introduced by discrete elements often used in the effective media. Fortunately, the thickness variation at the microscale and nanoscale has been achieved by advances in new manufacturing techniques, such as

microlithography and focused ion beam techniques. The effective refractive index of any transparent material, such as polymer (low refractive index) or silicon (high refractive index), depends on the thickness variation of the slab that guides the light.

In this work, the emphasis is on the effects of the geometry and refractive index of the microspheres on the resonances. Generally, the optical resonances in microrsonator are a function of morphology, meaning, their geometry and refractive index. Conditions required for WGMs to occur will be studied extensively. The coupled portion of the light that enters the sphere stays inside it, provided that the refractive index of the sphere is larger than that of its surrounding medium. The total internal reflection coupled with the matching conditions results in a resonance of certain wavelengths of the incident light inside the sphere. The solutions of Schrodinger-like equations in the spherical coordinates inside the sphere are expressed in terms of their radial and angular components or modes.

At first, we will treat MFE within a 2D model as a GRIN resonator. Starting from Maxwell equations the optical resonant modes of the structure are calculated both analytically and numerically.

The WGMs in optical microcavity resemble to the confined electron states in atoms. The WGMs contributing to photonic binding are always localized at the cavity surface, so they would be equivalent to atoms excited into high-energy orbitals. Due to these similarities optical microresonators can be termed as photonic atoms. On the other hand, clusters of circular cavities with coupled WGMs, several mutually coupled photonics atoms, form a photonic molecule.

There are examples of photonic molecule with plane discs in the literature. In second step of this wok, we assume the MFEs as the components of photonic molecule in linear chain and planer structures. The effect of mode splitting and mode hybridization are studied in these structures.

The optical resonators containing gain-loss materials implement platform that resemble the quantum systems with non-Hermitian parity–time (PT)-symmetric Hamiltonians. These resonators can provide asymmetric transmission. It means that different resonant modes of resonator can be exited depending on the input channel.

In optics, the PT-symmetry condition translated to the complex refractive index. In this work, we will study a new type of add-drop microring resonator made of gain and loss materials as a simple implementation of PT-symmetry in microphotonics.

The numerical method that we use in this work along the analytical solutions is Finite-difference time-domain (FDTD) method. We use the Meep, free software, and commercial FDTD software packages developed by Lumerical Company. The MATLAB will be used as usual simulation and calculation software.

ACKNOWLEDGEMENTS

First, I must give my sincerest thanks to my advisors Prof. Dr. Ramazan ESEN and Prof. Dr. Hamza KURT for all of their supports, guidance, suggestions, patience and encouragement on initiating, improving and completing this study. It was a great privilege to be their student.

I would like to thank to the members of my thesis committee Prof. Dr. Emirullah MEHMETOV, Prof. Dr. Hamide KAVAK for taking the time to read and comment on both my proposal and dissertation and Prof. Dr. Zeki YARAR and Asst. Prof. Dr. Mirbek TURDUEV for willing to serve in my committee and to Prof. Dr. Metin OZDEMIR head of the Department of Physics for his supports.

I would like to thank to our group members in TOBB ETU, Dr. Ibrahim H. Giden, Dr. Kadir USTUN, Emre BOR, Zeki HAYRAN, Bilgehan B. ONER, Melih G. CAN for their kind cooperation, and supports.

I would like to thank to Academic Research Projects Unit of Cukurova University providing support to this work.

Finally, my warmest thanks go to my wife, Leila and to my lovely daughter Katayoun. They were always there cheering me up and stood by me through the good and bad times.

CONTENTS **PAGE**

LIST OF TABLES **PAGE**

LIST OF FIGURES **PAGE**

LIST OF ABBREVIATONS

ABC	: Absorbing Boundary Condition
BCB	: Benzocyclobutene
CCW	: Coupled Cavity Waveguide
CQEM	: Cavity Quantum Electrodynamics
CROW	: Coupled-Resonator Optical Waveguide
EM	: Electromagnetic
FDTD	: Finite-Difference Time-Domain
FSR	: Free Spectrum Range
FWHM	: Full Width at Half Maximum
GRIN	: Graded Index
LDO	: Lenz–Demkov–Ostrovsky
MDR	: Morphology-Dependent Resonances
MFE	: Maxwell's Fish Eye
NMS	: Normal Mode Splitting
PA	: Photonic Atom
PBC	: Periodic Boundary Condition
PC	: Photonic Crystal
PM	: Photonic Molecule
PML	: Perfectly Matched Layer
PMMA	: Polymethyl Methacrylate
QED	: Quantum Electrodynamics
QW	: Quantum Well
RI	: Refractive Index
RIE	: Reactive-Ion Etching
SEM	: Scanning Electron Microscope
TE	: Transverse Electric
TM	: Transverse Magnetic

WDM : Division Multiplexing Application

WGM : Whispering Gallery Mode

1. INTRODUCTION

As the photonic devices, optical microresonators (or microcavities) have attracted increased attention in past decades mostly due to improvement in micro and nano fabrication technologies. These axially symmetric structures such as spherical, circular, ring, toroid and rectangular shaped microcavities can confine light to small volumes by resonant recirculation and select narrow part of the incident beam for further manipulation and processing (Tobing, Dumon 2010).

If we illuminate a circular structure laterally, it traps light in a small volume resulting in optical resonances in the transmission spectrum. These optical oscillations are known as whispering gallery modes (WGMs). The concept of WGMs is defined as circular electromagnetic waves supported by transmission from boundaries of the symmetrical structure. As a matter of course, these modes are morphologhy dependent, meaning depend on the geometry and refractive index of resonator and srounding medium. By using highly transparent, low scattering loss material, such as silica, the WGMs can provide extremely high values of Q-factor in a small mode volume. The Q-factor is mainly limited by the material attenuation and scattering loss contributed by surface roughness and geometrical imperfections. The high index difference at the boundary and relatively larger curvature (typically exceeds several wavelengths) guarantee the minimization of radiative loss and bending loss.

Devices based on optical microresonators are already indispensable for a wide range of studies and applications. These devices have been demonstrated to be important components in many applications. Some examples include single photon sources in cavity quantum electrodynamics (QED) applications, interfaces for quantum communications, microlasers, biosensing, optical circuits, dynamic filters and switches in optical communications (Vahala 2003).

On the other hand, graded index (GRIN) structures have been receiving great interest in recent years from invisibility cloaks and illusion devices, to planar

lenses, such as Maxwell's fish eye (MFE). These structures are inhomogeneous media with spatially varying refractive index distributions. Among GRIN structures, the MFE is of special interest and can be implemented using dielectric materials. (Dadashi et al 2014a). In this thesis, we study a new method for achieving high optical Q-factor on spherical dielectric microresonators. We have shown that, the GRIN approach can increase the Q-factor in comparison with typical conventional microresonators.

There are different approaches to fabrication dielectric microresonators. Microdisc or microtoroid can be made by photolithography and chemical etching (Zhu et al 2010). Microfluidic ring resonator is made by an etched cylindrical tube integrated with chemical fluid (Shopova et al 2007).

Fabrication of GRIN structures, where the dielectric medium is modified rapidly on a few-wavelength scale, is challenging and limited by scattering loses introduced by discrete elements often used in the effective media. Fortunately, the thickness variation at the microscale and nanoscale has been achieved by advances in new manufacturing techniques, such as microlithography and focused ion beam techniques. The effective refractive index of any transparent material, such as polymer (low refractive index) or silicon (high refractive index), depends on the thickness variation of the slab that guides the light.

After this introductory chapter, the thesis is organized as follows. Chapter 2 briefly introduces the general information and historical background of the optical microresonators. Theoretical and experimental works on microresonator is presented and the advantage and limitations are analyzed. Also in this chapter, the historical background of Photonic Atoms (PAs) and Photonic Molecules (PMs) will be discussed.

The main device for this thesis is MFE, on which the optical properties are analyzed and analytical and numerical techniques are discussed. In chapter 3, first the necessary numerical tools for the study of the structures are presented. The finite-difference time-domain (FDTD) method is presented in this chapter. Also, an

introduction to optical microresonators, different aspects of them, such as their geometry, quality factor (Q-factor) and free spectral range (FSR) are introduced.

In chapter 4 we theoretically investigate optical characteristics of 2D MFE. The emphasis is on the effects of the geometry and refractive index of the microspheres/microdiscs on the resonances. Starting from Maxwell equations the optical resonant modes of the structure are calculated both analytically and numerically. The solutions of Schrodinger-like equations in the spherical coordinates inside the sphere are expressed in terms of their radial and angular components or modes. Through our numerical calculations, the FDTD method is used. A detailed analysis section is included to study Q factor and FSR

Chapter 5 of this thesis considers the structure studied in the previous chapter, MFE, as a Photonic Atom (PA). The WGMs in optical microcavity resemble to the confined electron states in atoms. The WGMs contributing to photonic binding are always localized at the cavity surface, so they would be equivalent to atoms excited into high-energy orbitals. Due to these similarities optical microresonators can be termed as photonic atoms. On the other hand, clusters of circular cavities with coupled WGMs, several mutually coupled photonics atoms, form a photonic molecule (PM).

In chapter 6 we study a new type of add-drop microring resonator made of gain and loss materials as a simple implementation of PT-symmetry in microphotonics. The relevant references are listed thereafter.

The numerical method that we use in this thesis along the analytical solutions is FDTD method. We use the MEEP, free software. The MATLAB will be used as usual simulation and calculation software.

2. REVIEW OF LITERATURE

Optical microresonators have gained a great prominence as fundamental building blocks for a variety of applications in photonics. Functionally similar to Fabry–Perots resonator, optical microresonators can take the form of closed shapes such as ring, disc, racetrack, ellipse, or sphere and cylinder with a common feature that there exists a curved boundary which refocuses the propagating field (see Figure 2.1). The confinement of light in these closed geometries, however, does not require an inner dielectric boundary. This is evidenced by the existence of optical whispering gallery modes (WGMs). Placement of a microresonator near a waveguide enables access to modes of the resonant cavity. In this particular arrangement, the resonant modes are accessed through evanescent coupling, phenomena analogous to tunneling in solid-state physics (Heebner et al 2008).

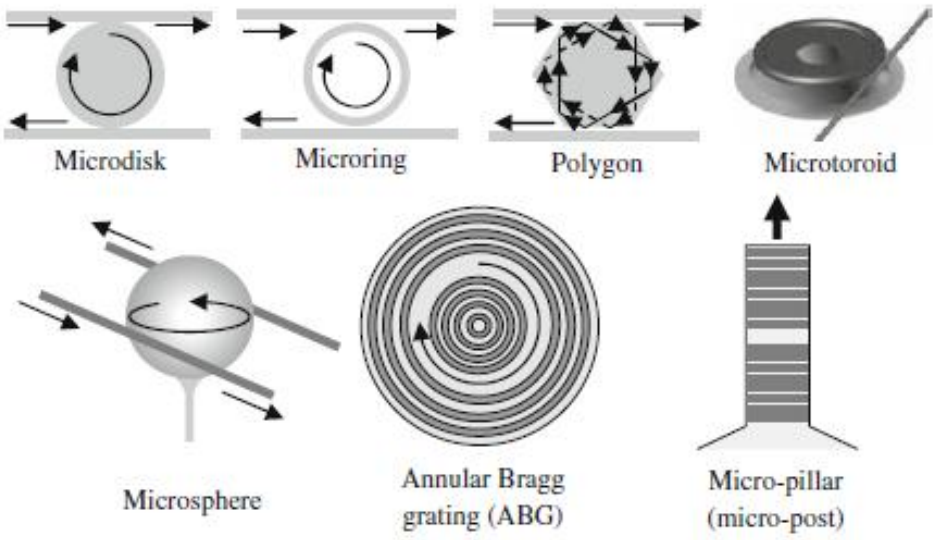

Figure 2.1. The various forms of photonic microresonators (Tobing, Dumon 2010).

The history of optical microresonators starts with the physical explanation of whispering gallery effect as early as 1910 by Lord Rayleigh. His analysis of the channeling of acoustic waves by the dome of St. Paul's cathedral in London is a first step to similar methods applied to electromagnetic waves. It was known that a sound (a whisper) uttered at one end of the dome could still be heard loudly at the opposite end of the dome, a large distance away from the source. Lord Rayleigh described this phenomenon by noting that sound seemed to "stick" to the dome's walls and propagate only inside a narrow layer near the surface of the concave wall of the gallery (Oraevsky 2002) (see Figure 2.2).

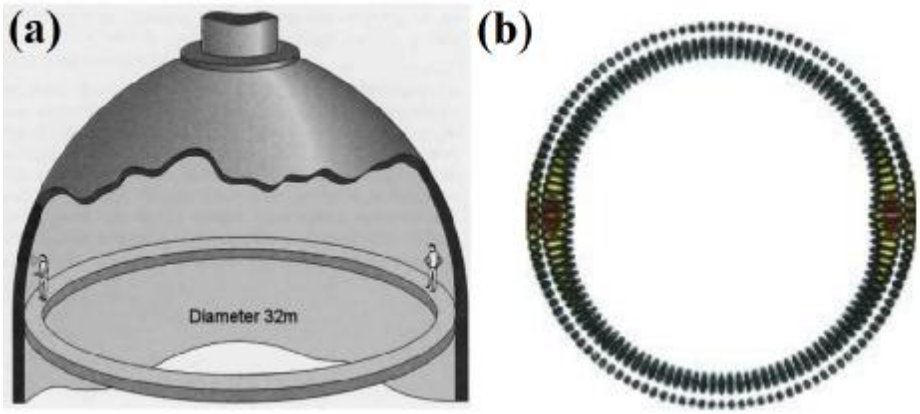

Figure 2.2. (a) Whispering gallery under the dome of St. Paul's Cathedral in London. (b) The sound intensity profile showing the whispering gallery phenomenon that Lord Rayleigh studied. (Oraevsky 2002)

In the early 1960s, ring and disc resonators have been implemented in microwave applications for electromagnetic waves. In the optical domain, integrated ring resonators were proposed by Marcatili (1969) at Bell Labs. Marcatili studied light transmission through closed dielectric rod of rectangular cross section. He studied the relations between radiation losses resulting from curvature, geometry, and electric characteristics of the bent dielectric guide. For a given radius of curvature R, he analytically showed the radiation loss can be

reduced (i) by increasing the difference between the refractive index of the guide, n_1, and those of the media toward the outside, n_3, and inside, n_5, of the curved guide axis (see Figure 2.3); (ii) by increasing the guide width a (iii) by choosing the height of the guide large enough to confine the fields as much as possible within the guide in the direction normal to the plane of curvature (Marcatili 1969).

In another work at Bell Labs, Weber and Ulrich (1971) demonstrated the first optical ring resonator. They reported the operation and characteristics of a ring laser formed by a single-mode lightguiding thin film. The Rhodamine-6G-doped polyurethane ($n = 1.55$) film was coated on the surface of a cylindrical glass rod ($n = 1.47$). The geometry established feedback for laser oscillation around the circumference of the rod. A N_2 laser (λ = 337.1 nm) served as pump source. Light was coupled in and out of the resonator with a prism (see Figure 2.4). A 0.8 μm-thick film of polyurethane, doped with Rhodamine-6G, was coated on the outside of a glass rod of 5 mm diameter. The beam of a N_2 laser was focused into a line, pumping a narrow section of the rod. The resulting laser light traveled around the rod. It was coupled out by a prism, which was in loose contact with the rod. The two output beams corresponded to clockwise and counterclockwise oscillation of the ring laser (Weber and Ulrıch 1971).

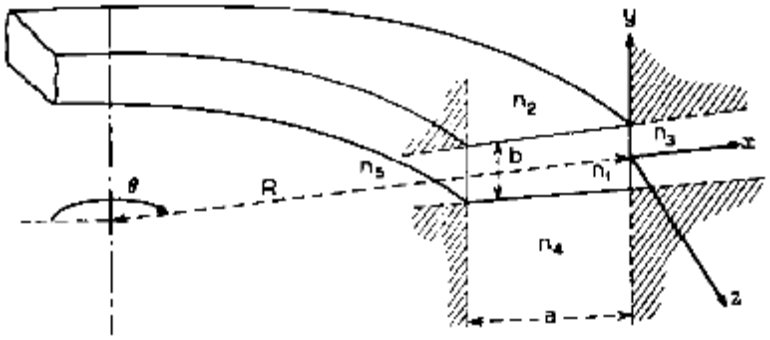

Figure 2.3. Closed dielectric waveguide (Marcatili, 1969).

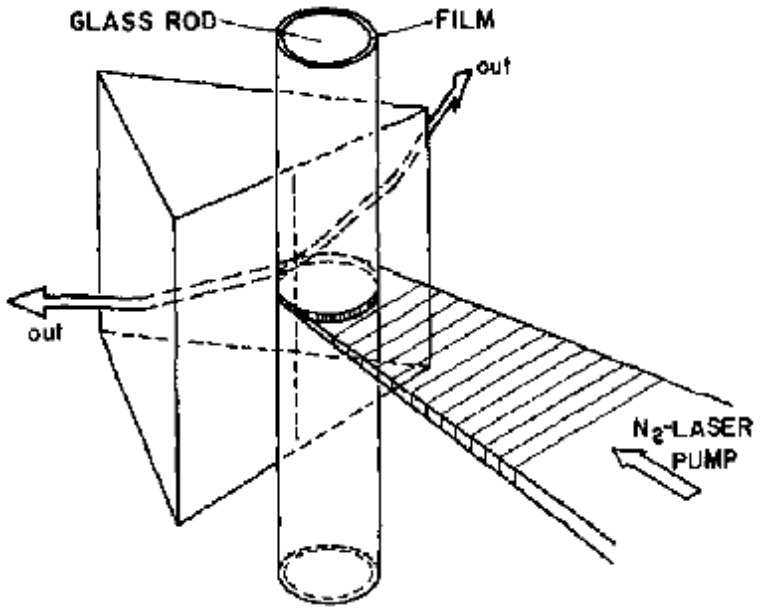

Figure 2.4. The first ring-laser arrangement (Weber and Ulrıch 1971).

Haavisto and Pajer (1980) demonstrated the first low-loss channel waveguides in a ring-resonator configuration. The waveguide structure of the thin-film resonator was fabricated by the photopolymerization of doped polymethyl methacrylate (PMMA) films. The substrate was quartz disc of 13 cm diameter and the radius of the ring was 4.5 cm (see Figure 2.5). This low-loss structure enabled a substantial improvement in the evaluation of the characteristics, particularly losses, of channel waveguides. In their fabricated structure total losses, including coupling, material, bending, and fabrication losses, were 0.05±0.01 dB/cm. Although they offered an alternative to existing fiber-optic hybrid devices, but the ring was quite large (circumference 28.3 cm). The significant feature of this work was that the device was fabricated without lithography by using direct-writing with a 325 nm He–Cd laser (Haavisto and Pajer 1980).

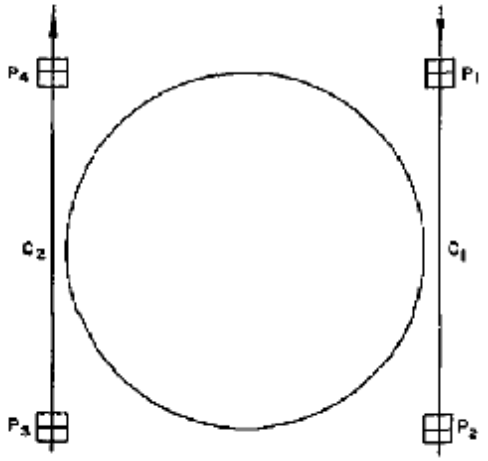

Figure 2.5. Ring-resonator configuration with input-output prism couplers (P_1-P_4) and evanescent-wave couplers (C_l,C_2). Two tangential straight channel waveguides serve as evanescent-wave input and output couplers. Prism couplers (P's) are used to couple light in and out of the resonator. (Haavisto and Pajer 1980).

The first optical glass fiber ring resonator, operating at λ = 632.8 nm, was demonstrated by Stokes, Chodorow, and Shaw by using a single strand of single mode optical fiber and a directional coupler in 1982. They used a single mode optical fiber to make a high finesse optical resonator by forming a short piece of fiber into a closed ring to form a low loss cavity. A fiber resonator of length L=3 m was fabricated from ITT fiber having a 4 μm core diameter. A single frequency, long coherence length He-Ne laser (λ = 632.8 nm) was used to excite the resonator (Stokes et al 1982).

Up to 1982, the ring resonators had been made for use at microwave frequencies and their design had been considered by a number of authors (Heebner et al 2008). Optical filters were required for a number of purposes in optical communication systems. For compatibility with optical fibers, such filters should be constructed from stripe waveguides. Walker and Wilkinson demonstrated a ring resonator with dimensions suitable for optical communications (Walker and Wilkinson 1983). The waveguides used for the fabrication of the ring resonators

(with circumference of 3.1 mm and operating at λ = 632.8 nm) were made by silver-sodium ion-exchange in substrates of soda-lime glass. In the similar work Connors and Mahapatra demonstrated a ring resonator with circumference of 4.1 mm and operating at λ = 632.8 nm in 1986 (Heebner et al 2008).

In 1984, Honda, Garmire and Wilson reported observation of resonance in a ring waveguide. They wanted to study the possible application of the passive ring resonator to inertial rotation sensing, for this reason the resonator consisted of an integrated optics ring fabricated with a diameter as large as possible (4 cm in diameter). Coupling onto and off of the resonant ring was provided by adjacent straight channel waveguides acting as directional couplers. The waveguides were fabricated by potassium ion exchange in commercially available soda lime glass substrates (Honda et al 1984). The geometry which they used was very similar to Figure 2.5.

Ring resonators in lithium niobate were particularly appealing because of the possibility of electro-optic tuning. Such a resonator using directional couplers and Ti-diffused guides demonstrated by K. H. Tietgen in 1984. Tietgen represented the first demonstration of a tunable ring resonator. Instead of a circular ring, he used a waveguide loop with two 3 dB couplers. His device used electro-optic tuning, had a circumference of over 24 mm, and operated at λ = 790 nm (Heebner et al, 2008).

Proton exchange in lithium niobate using benzoic acid permits a large Δn. Moreover, proton exchange provides guided modes for only the extraordinary polarization state. For that reason, the fabrication of ring resonators made by proton exchange in lithium niobate has gained attention of Mahapatra and Robinson (Mahapatra and Robinson 1984). They used the racetrack configuration as shown in Figure 2.6. The mask was fabricated using an e-beam pattern generator with a spot size of 0.25 μm. So, the maximum sidewall roughness and lateral offset of the guides was 0.25 μm. This resulted in significant scattering losses, since the waveguides were only 2 μm wide. The device was fabricated on Z-cut $LiNbO_3$.

The ring structure was defined on a 800-Å layer of chromium with the proton exchange. Channel guides were found to support two or three TM modes (Mahapatra and Robinson 1984).

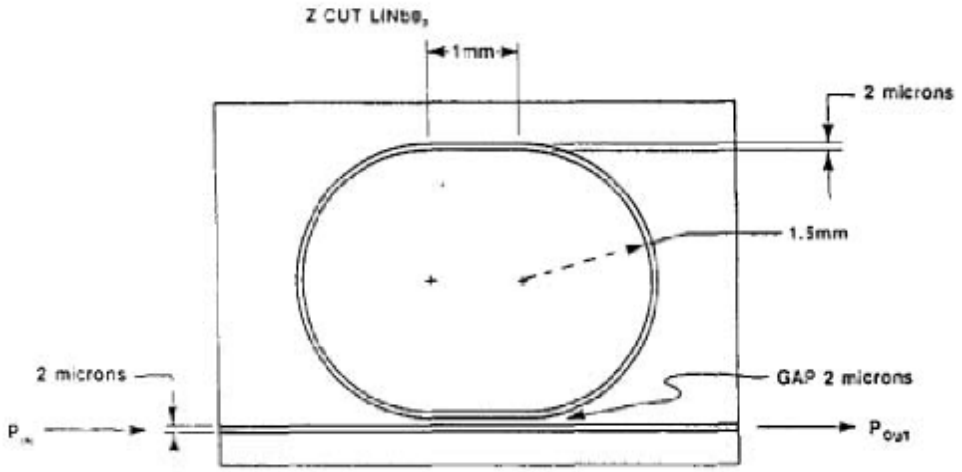

Figure 2.6. A schematic of the resonator using the racetrack configuration (Mahapatra and Robinson 1984).

In 1997, Rafizadeh et al stepped up an important step toward developing photonic integrated circuits. They demonstrated nanofabrication methods of semiconductor waveguide-coupled microcavity ring and disk resonators. They studied 10.5 and 20.5 mm in diameter AlGaAs/GaAs ring and disk microcavity resonators which are the smallest ones at that time.

Alongside various doped and undoped silica-based glasses and Si-based component, there have been some works in electrooptic polymers. Because of the wide range of indexes of refraction, polymers are suitable materials for microresonators. The maximum index difference of available polymers is 0.3. Polymer films are simple to fabricate as the various polymer layers can be spin-coated, and other layers can be deposited with chemical vapor deposition. They can be easily patterned by photo processing. Moreover, polymers can be engineered to

have desirable properties by doping them with appropriate materials, or whole new polymers can be designed. They are resilient and can withstand a lot of abuse without breaking (Chen et al 2003). Vertical coupling is well suited to the polymer technology because of the ease of fabricating in different layers and the range of indices available.

The first polymer microresonators have been introduced by Rabiei et al in 2002. They reported the first work using polymers in both passive and active microresonators (Rabiei et al 2002). Rabiei et al fabricated two different sets of devices; one set with an index difference of 0.1 and radius greater than 220 μm, and a second set with an index difference of 0.3 and radius greater than 25 μm. The fabrication of the device had several levels using polymer materials. First, a Teflon film was coated with spin coating method on silicon substrate. Then the film was etched using reactive-ion etching (RIE). In the next steps, by using lithography, coating and etching methods the ring, input and drop waveguides were formed (Rabiei et al 2002). In addition, another group at the University of Maryland demonstrated polymer microring and microracetrack resonators made from benzocyclobutene (BCB) microrings (Chen et al 2003). They demonstrated optical channel dropping filters with a variety of FSR's by varying the resonator circumference. Their devices were among the smallest radius (10 μm) and widest FSR (18.25 nm) for this class of devices. Further, the first microresonators made from BCB, which is a popular low-cost polymer for photonics applications were introduced.

Another class of WGM microresonators was based on III-V semiconductors. There are, of course, many demonstrations of microresonators from various groups, each employing slightly different approaches. In 1993, Chu et al reported the demonstration, for the first time, of a microdisc laser in the InAlGaAs-InGaAs quantum well (QW) material system. The microdisc was formed by the selective etching method. This material system, with widely tunable bandgap energy could be used as optical window in fiber optic communications. In

fact, the achievement of microdisc lasers in these material systems had potential application for optical communication systems (Chu et al 1993). For such microdisc laser with 20 μm diameter, the lasing demonstrated at single mode at 1.5 μm under pulsed excitation with 518 nm Argon-ion laser at low temperature, 80ºK. The laser threshold intensity was four times higher but mode area is 12 times larger than former systems. That, in turn, provided the higher trap density and surface recombination in this material system.

Most of early works in 1990s did not incorporate bus waveguides and relied on fibers to directly couple to and collect light from the disc. The first GaAs-AlGaAs resonator laterally coupled to bus waveguides was demonstrated by Rafizadeh et al in 1997 (Heebner et al 2008) as an important step toward developing photonic integrated circuits. They reported the demonstration of semiconductor waveguide-coupled microcavity ring and disc resonators. The scanning electron microscope (SEM) images of microresonators are shown in Figure 2.7. They used nanolithography methods to fabricate and demonstrate waveguide-coupled 10.5mm and 20.5-mm-diameter ring and disk microresonators. The adjacent waveguides were 2 μm wide at each end and gradually taper to 0.5 mm near the ring or disc. Thus, the ratio of the waveguide width to disc and ring radii was about 0.1 in the coupling region. The waveguide structure was grown upon a GaAs substrate by molecular-beam epitaxy. The key microcavity resonator design parameters were the coupling efficiency and the waveguide propagation loss (which was mainly due to sidewall roughness). Strong waveguiding confinement dictated at the resonator-to-waveguide gap has to be very small for adequate evanescent coupling. . Based on the limits of the nanofabrication technology at that time, the fabricated gap widths was 0.1 μm (Rafizadeh et al 1997).

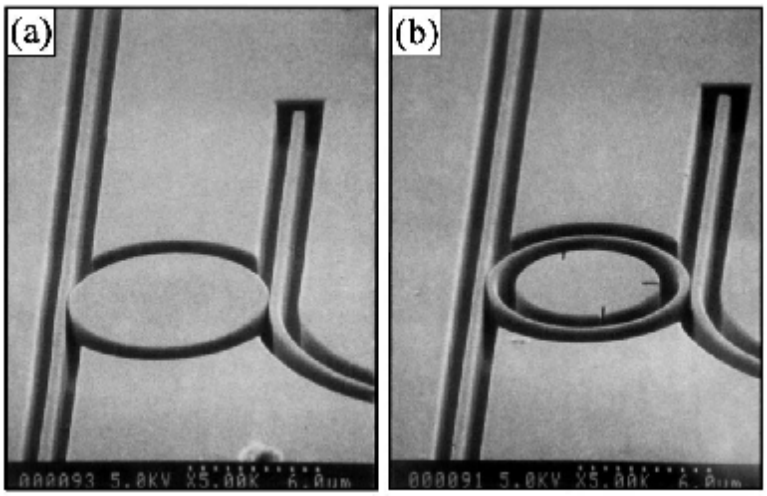

Figure 2.7. SEM images of a 10.5-μm-diameter (a) disk and (b) ring. (Rafizadeh et al 1997).

The developments on fabrication of high quality solid state structures with sizes on the scale of the wavelength of light made it possible to modify the interaction between light and matter within a single solid state system. These systems, some known optical microresonators, enhanced the study of confined photon properties such as that of the detailed works had been done on confined electron states in nanostructures (Bayer et al 1998). Optical microresonators can be termed photonic atoms (PAs). Controllable interaction between light and matter in microresonators can be further modified and enhanced by the manipulation of their mutual coupling. These coupled microresonators introduce new terms in photonics: Photonic molecules (PMs).

Theoretical studies carried on for over two decades have provided novel PM designs. Such type of configurations provides lowering thresholds of semiconductor microlasers, producing directional light emission, achieving optically induced transparency and enhancing sensitivity of microcavity-based sensors. Photonic molecules are photonic structures formed by electromagnetic coupling of two or more PAs (Boriskina 2010). Stephen Arnold et al were the first to introduce the term photonic atom in 1992. In a two dimensional distribution of

spherical dielectric particles on a glass surface, known as a microparticle hole burning medium, they showed the differences in the frequencies of morphology-dependent resonances (MDRs) with size enable one to generate a fluorescence excitation spectrum that is inhomogeneous (Arnold et al 1992). In their previous work, they had presented a means for encoding information into such a distribution of particles in room temperature that takes direct advantage of the narrow MDR's of microparticle. For the case of the fluorescence excitation spectrum taken on an ensemble of dyed microspheres, their work was based on two facts: A given MDR occurs at a wavelength in proportion to the particle's size (with the refractive index held constant). The second one, the spectrum is composed of the sum of spectra from individual particles, each with resonances that appear at different wavelengths. So, a collection of particles having a distribution of sizes gives rise to a photophysical response that is inhomogeneous. Thus, the normal homogeneously broadened excitation spectrum of a typical dye at room temperature is found to become inhomogeneous for measurements on an ensemble of dyed particles. Furthermore, electrodynamical calculations for a pair of particles in contact provided an explanation for the apparent lack of importance of interparticle interactions. By disregarding the interactions between particles, even though each particle in the distribution touched at least one of its neighbors, they made interpretation for the experimental results.

The first demonstration of a lithographically fabricated PM was inspired by Bayer et al in an analogy with a simple diatomic molecule (Bayer et al 1998). They reported studies of the optical modes in molecule-like structures made from pairs of interacting photonic dots which had been coupled by narrow channels. They studied optical modes in these structures as a function of the coupling and the mode energies were compared to detailed calculations. The confined photon modes had been studied by photoluminescence spectroscopy as functions of the coupling which could be varied through the structure design. They found that the optical

modes in photonic molecules can exhibit strong similarities to those of electronic states of diatomic molecules.

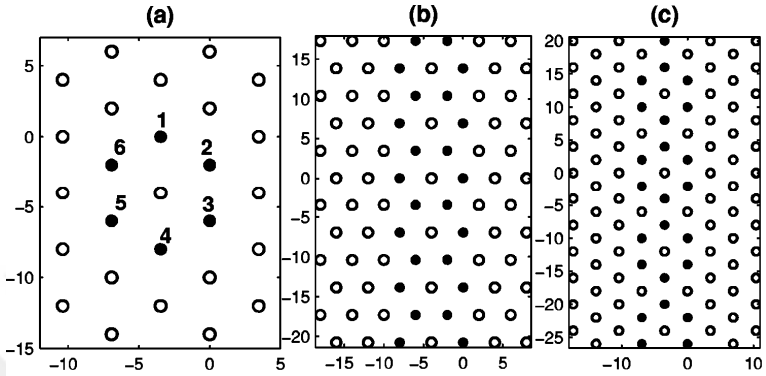

Figure 2.8. Formation of (a) photonic benzene, (b) benzene WG of π type, and (c) benzene WG of σ type in a 2D hexagonal photonic crystal; each solid dot denotes a defect atom of radius r (Lin 2003).

In 2003, Lin proposed an artificial nature-inspired PM structure. It consisted of coupled-defect atoms in a 2D photonic crystal. Lin theoretically presented a method to determine the frequency of each resonant mode for the PM. He showed that the confined optical modes, within the major band gap, are closely analogous to the ground-state molecular orbitals of their chemical counterparts and the corresponding electromagnetic spectrum is also isomorphous to the electric energy levels (Lin 2003). Figure 2.8 (a) shows a 2D photonic molecule named as the photonic benzene. In the second part of his work, Lin proposed a new type of photonic waveguide for the two-dimensional systems. Before his work, the formation of conventional photonic waveguides generally was considered as the arrangement of the desired defect atoms along a line. However, this approach had limited the potential of development. Instead of a line defects in photonic crystals, the defect atoms were closely arranged to form a structure that is similar to a real molecule. Figure 2.8(b)-(c) shows two type of 2D benzene waveguide. In particular, manipulating the mechanism of photon hopping between photonic

benzenes can provide the function of guiding photons along the benzene chain with a very high transmission, and presents an optical feature of twin waveguiding bandwidths in the 2D system.

In 1999, Prof. Yariv and his colleagues introduced a new type of optical waveguide, coupled-resonator optical waveguide (CROW) that consists of a sequence of coupled resonators (See Figure 2.9(c)). Two mechanisms had been used in the past for optical waveguiding. Waveguiding by total internal reflection and Bragg waveguiding, in which waveguiding is achieved through Bragg reflection from a periodic structure as illustrated in Figure 2.9 (a)-(b). Unlike these types of optical waveguide, waveguiding in CROW is achieved through weak coupling between otherwise localized high-Q optical cavities. Figure 2.9(c) shows a possible realization of such a waveguide based on evanescent-field coupling between the high-Q WGMs of individual microdisk cavities. Employing formalism similar to the tight-binding method in solid-state physics, Yariv et al obtained the relations for the dispersion and the group velocity of the photonic band of the CROW's and found that they are solely characterized by coupling factor. They also demonstrated the possibility of highly efficient nonlinear optical frequency conversion and perfect transmission through bends in CROWs. In realization of the CROW they assumed sufficiently large separation between the individual resonators. Consequently, the eigenmode of the electromagnetic field in such a coupled-resonator waveguide remain essentially the same as the high-Q mode in a single resonator. At the same time one must take into account the coupling between the individual high-Q modes to explain the transmission of the electromagnetic waves. This coupling is exactly the optical analog of the tight-binding limit in condensed-matter physics, in which the overlap of atomic wave functions is large enough that corrections to the picture of isolated atoms are required yet at the same time is not large enough to render the atomic description completely irrelevant. The individual resonators in the CROW are the optical counterpart of the isolated

atoms, and the high-Q mode in the resonators corresponds to the atomic wave function (Yariv 1999).

For device applications in photonics, the structures where photons can be trapped for long time without losing their energy are highly desirable. In all-optical switching devices, optical storages in optical routing systems and quantum repeaters in quantum information processing and communication, as active systems, a scheme to decrease light velocity with a strictly loss-free mechanism is essential. However, preparing lossless medium for these device applications are limited because of the extreme precision required in the manufacturing. Therefore it is important to develop a passive system which significantly decreases the speed of light (Hara et al 2005).

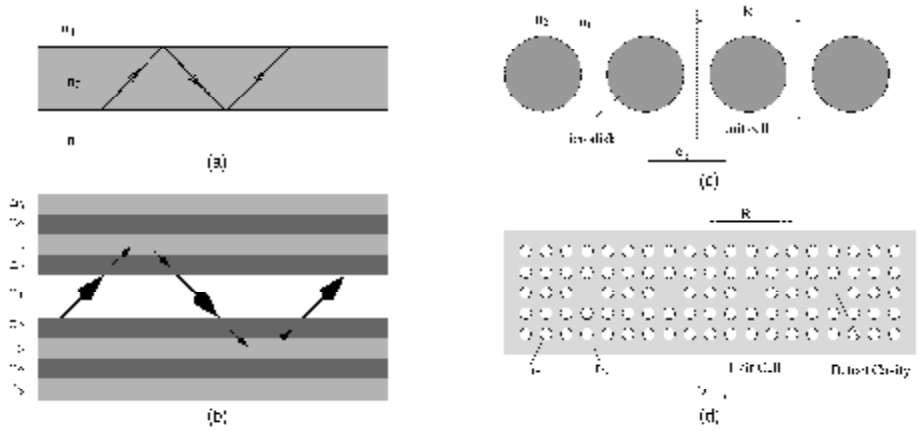

Figure 2.9. Three types of waveguiding: (a) waveguiding achieved through total internal reflection at the interface between a dielectric medium with a high refractive index n_2 and a low refractive index n_1. (b) Bragg waveguiding achieved by reflection from periodic Bragg stacks. (c) CROW, with waveguiding that is due to coupling between individual microdisks. ***R*** is the size of a unit cell, and e_z is the direction of the periodicity for the coupled resonators. (d) CROW realized by coupling of the individual defect cavities in a 2D photonic crystal. ***R*** and e_z are defined the same as in (c) (Yariv et al 1999).

At the last decades of twentieth century, manipulation of light path in micrometer length scale was mostly based on the photonic crystal concept. Photonic crystals, artificially manufactured materials having a periodic dielectric constant, have periodic modulation of the refractive index. Nearly free photon approach, analogous to the nearly free electron approach in band theory and tight-binding photon approach analogous to tight-binding approximation in solid state physics successfully used in photonic crystals. The idea of using tight-binding approach in PMs was offered by Mukaiyama et al in 1999. The manipulation of light can be achieved by confining of light in a small unit of the wavelength size. Light propagates through the system of such units due to the coupling between the nearest neighbors. This approach is referred to as the tight-binding photon approach. Within the tight-binding photon approach the optical waves can be guided by connecting the units in the arbitrarily shaped microstructures (Mukaiyama et al 1999). The microspheres are the most natural choice of the unit to be employed in the tight-binding photon device. It is known that a dielectric sphere acts as a unique optical microcavity which has very long photon storage time within a small mode volume (Mukaiyama et al 1999). The coherent coupling between two adjacent small microspheres of diameters ranging from 2 to 5 μm has been realized for first time by Mukaiyama et al. Such relatively small spheres can be employed as PAs for the tight-binding scheme. On the other hand, the coherent coupling results in the splitting of the corresponding WGMs is a manifestation of the normal mode splitting (NMS) in coupled harmonic oscillators. Although some attempts had been made, because of the difficulty in the precise size control of the spheres NMS had not been observed yet. Mukaiyama and his colloquies reported the observation of normal mode splitting in the system of two polymer spheres in contact (bisphere) under extreme size control. In order to make the bisphere, they chose two spheres of the desired size by comparing the frequencies of the specific WGM resonances. The frequencies of the observed bisphere resonances agreed with the wave optics calculations.

In another work from previous research group, Hara et al could design and construct a linear molecule as a chain of coupled PAs composed of size-matched microspheres placed in a V groove on crystalline silicon (Hara et al 2005). They studied the spectral finger-prints of linear molecules by combining the tight-binding photonic description with the wave-vector quantization due to periodic boundary conditions. Actually, the propagating modes with slow group velocity of defect or edge modes of photonic crystals, which are referred as heavy photon modes had been studied by formers. But the group delay in such modes in photonic crystals is limited by its bandwidth. The new proposed coupled cavity waveguides (CCWs) composed of three dimensional high quality factor microcavities had the potential to remove this limitation. In CCWs, trapped photons in a microcavity can tunnel to a neighboring cavity. The CCW structures with many attractive features had been faced major technological difficulties that time. The fabrication of such structures required extreme accuracy and reproducibility, beyond the limit of microfabrication technology of ten years ago. So, Hara et al proposed and realized a bottom-up method to construct a CCW structure to overcome these difficulties. Polystyrene spheres of 4.2 μm in diameter doped with Nile Red (refractive index 1.59) were used. They used a Q-switched Nd-YLF laser on its second mode with a wavelength of 527 nm, a repetition rate of 1 kHz, and pulse duration of 300 ns as a pump light source. At the end, they found that a photonic band is formed due to the resonant coupling of nearest-neighbor WGMs and it is in excellent agreement with a coupled oscillator tight-binding model. They also demonstrated that the structures have a strong potential for an optimal control of photons in the visible region (Hara et al 2005).

In 2000, Miyazaki and Jimba applied ab initio tight-binding formalism in bisphere PM. Their work opened up a new possibility to describe MDRs by the tight-binding model. They showed that the energy spectra reveals the fine structure of the bonding and antibonding branches originating from the Mie resonance of a single sphere. The formation of bonding and antibonding states can be deduced

from electric field distribution. Miyazaki and Jimba used this detailed information of resonance in a bishpere. In analogy to the quantum-mechanical formation of the molecular orbits, it is expected that the interaction between spheres brings about the bonding and antibonding states of the electromagnetic field. These states can be expressed as a linear combination of the Mie resonance states of each sphere. Before this work, Fuller had observed numerically that the electromagnetic coupling between spheres causes the narrow Mie resonance to split into distinct, relatively broad peaks and dips in the forward-scattering spectrum of the bisphere (Fuller 1991). Also, in the photoluminescence study of the photonic molecule made from a pair of photonic dots coupled by narrow channels, it had been found that the optical modes in photonic molecules exhibit strong similarities to those of the electronic states in diatomic molecules (Bayer et al 1998). Miyazaki and Jimba, wanted to determine accurately the positions of MDR's by using the internal energy spectra. The internal energy plays a crucial role in lasing because it gives a direct measure of the quality factor Q. Based on the vector spherical harmonics expansion, they got a simple and handy tight binding equation that clarified the meaning of the overlap integral. In addition, it gave almost all the qualitative explanations of the characteristic features of MDRs in a bisphere. In their approach the overlap integral could be evaluated exactly. In this sense, they called the formalism as the ab initio tight-binding model (Miyazaki and Jimba 2000).

Rakovich and Donegan provided a survey of PAs and PMs in 2010, after thier some works in the issue. By considering the analogy of Mie resonances (WGMs) of a single spherical microcavity with atomic orbitals in a hydrogen atom, they introduced the mode numbers of microcavity. The eigenfunction for the electron confined in the hydrogen atom and electromagnetic fields confined in a microsphere are very similar. So, in the absence of gain, they could characterized WGM resonances by a mode number n (angular quantum number), a mode order l (radial quantum number), and an azimuthal mode number m (azimuthal quantum number). The value of n is proportional to the circumference divided by the

wavelength of the light propagating within the microsphere, the mode order *l* indicates the number of maxima in the radial distribution of the internal electric field, and the azimuthal mode number m gives the orientation of the WGMs orbital plane (Rakovich and Donegan 2010). Also, they stated that, unlike energy states of electrons in the atom, photonic states in spherical microcavities are not localized, due to the finite storage time of photons in the resonant mode. This time, named as photon lifetime, is controlled by quality factor Q of the WGMs and therefore can be limited by diffractive losses, absorption, gain, shape deformation or refractive index inhomogeneities. As a result, the resonant internal field of a spherical cavity is not completely confined to the interior of the microparticle. Depending on the size of the microsphere, the evanescent field can extend into the surroundings up to a couple of micrometers permiting efficient coupling of microcavities. This partial delocalization of Mie resonance states (WGMs) suggests the possibility for coherent coupling between WGMs of two adjacent spherical particles with closely matched sizes, a main step from PAs to PMs (Rakovich and Donegan 2010). One another point has been noticed these researchers, is complex internal distribution of the density of photonic states of the PM originating from lifting of the degeneracy of PM modes with respect to the azimuthal mode number *m*.

Almost the last article on PAs and PMs was published by Li et al in 2017. Again, by considering the analogy between quantum mechanics and the classical electrodynamics, they assembled dielectric microspheres as classical photonic atoms, and sorted them in a wide range of structures to form linear chains and planar PMs. They studied WGM hybridization in such PMs theoretically and experimentally. The numerical simulation was performed in the 2-D case corresponding to the equatorial cross section of the 3-D structures. Li et al studied various structures, 3-sphere and 4-sphere chain molecules, quadrumers, 5-atom crosses and hexamers. They observed that PMs have certain spectral properties which are closely related to the topology and geometry of a given molecular configuration. The number of atoms determines the number of spectral components

which can be split or degenerate depending on the symmetry. They introduce the spectral signature of PMs, as a result of WGM hybridization effects. They showed that the splitting/ hybridization of WGM modes are dependent on the symmetry, number of constituting atoms and topology of the photonic molecules which in principle can be viewed as spectral signatures of various molecules (Li et al 2017). In order to find the spectral signature, the simulations were performed for three different combinations of the structural parameters, the refractive indices n, diameters D of microspheres and surrounding media (air or water). They chose the diameter of circular resonators 7 and 25 μm, the refractive index was varied from 1.59 to 1.9, and the medium was changed from air to water (Li et al 2017). Strong coupling and mode splitting are observed in every case. According to their FDTD simulations, Li et al found that the splitting patterns of supermodes were quite similar even though the diameter of circular resonators is varied from 7 μm to 25 μm, their index was varied from 1.59 to 1.9, and the medium was changed from air to water. Also, each photonic molecule with a particular configuration and symmetry had unique resonant properties that give rise to its distinct spectral signature. This can able one to identify the molecule configuration based on its spectrum, giving the ability to potentially utilize such signatures for geometry or position sensing. In the E-field map, the shortest and longest wavelength components can be called antibonding and bonding modes, respectively. For antibonding mode, they found that the electric field appears to be distributed rather uniformly among all constituent atoms, which is not seen in other modes. Also, the E-field is reduced at the points where the circular resonators touch which means that the coupling at these points is weakened. To experimental study of spectral properties of photonic molecule, Li et al assembled various molecular configurations with polystyrene microspheres with nominal diameter of 25 μm and similar resonant positions of WGMs. The positions of the WGM resonances were determined using transmission spectra through side coupled tapered fiber in aqueous environment. Liquid environment enables particle movement and is

critical for developing biomedical applications, thus most of WGMs based sensors are characterized in an aqueous medium. This novel work opens up a way to explore quantum-optics analogies in photonics and to create novel structures such as parity-time synthetic lattices, coupled resonator ladders or waveguides based on an effective gauge field for photons (Li et al 2017).

In the following chapters we study Maxwell fish-eye (MFE) as a graded index (GRIN) microresonator. The history of this newly considered structure came back to the middle of 19th century. In 1854, seven years before declaration of the electromagnetic theory of light, James Clerk Maxwell invented MFE based upon the method of geometrical optic. A spherically symmetric inhomogeneous lens which refractive index is a function $n(r) = 2n_0 /(1+(r^2 / R^2)$, where R denotes the radius of the sphere, and r the radial distance measured from the center of sphere (Tai 1958). At first, the MFE problem was an unbounded i. e. $n(r) = n_0$, for r **f** R but in recent works it is assumed $n(r) = 1$, for r **f** R.

The wave equation for this problem can be reduced to the Laplace equation on a four-dimensional sphere. The symmetry group for this problem is, therefore, the same as that found by Fock for the hydrogen atom in the case of the discrete spectrum.

The similarity between light rays in MFE and the trajectories of a particle of mass *m* in the attractive potential was realized by researchers. In 2009 Makowski offered a normalizable solution for Schrodinger equation at the energy of E=0 and compared the results to the corresponding classical trajectories. His model was a specific version of the MFE. Before Makowski's work, Lenz for the refractive index and Demkov and Ostrovsky for the corresponding potentials, had shown that there exist a large class of functions $n_k(r)$ and $V_k(r)$ with the perfect focusing properties. The Lenz–Demkov–Ostrovsky (LDO) focusing potentials had the form of $U_k(r) = - w / 2R^2 r^2 (r^{-k} + r^k)^2$, r @/ R and for all rational

values of k lead to regular zero-energy quantum solutions. The MFE model is recovered for $k=1$. In each case, there exist normalizable solutions, if the coupling constant w is a quantized quantity. Makowski proposed another model which, contrary to the LDO potentials, was not central but could be related in some relation to the MFE case, i. e., to the question of finding focusing effects in media, where the refractive index or the corresponding to it potential, vary continuously with the radial coordinate. The model had square-integrable $E=0$ wave functions and also gave its exact classical trajectories (Makowski 2009).

In 2009 Leonhardt proved that MFE, as an ideal optical instrument, perfectly images light waves in two dimensions (Leonhardt 2009). Then in another work in 2010, Leonhardt and Philbin showed that the MFE in three dimensions has infinite resolution as well. They proved perfect imaging in three dimensions and obtain the quantitative results of Leonhardt 2009 by analyzing the electromagnetic Green function. In their theory having absorption is equivalent to having a complex wave number in the definition of the Green function. The singularities of the Green function describe source and image, but they are not affected by the wave number that only reduces the amplitude (Leonhardt and Philbin 2010).

3. MATERIAL AND METHOD

In this chapter, the numerical technique which is widely applicable for analysis of broad class of structures is presented. Since the last decades of twentieth century, the processing power and memory capacity of high-speed computers increases by the year. So, the solutions of electromagnetic (EM) field problems have been changed from contentious equations to discrete approximations. The discrete forms are usually easier to implement in computers (Buchanan 1996). These methods directly give the total picture of a field as it propagates through a structure involving several variations in physical characteristics. Among discrete approximations, the numerical analysis and simulation in the time-domain has been interested rather than frequency-domain. There are a number of finite-difference schemes for Maxwell's equations, but Yee scheme, known as Finite-Difference Time-Domain (FDTD) Method, persists as it is very robust and versatile.

3.1. Finite-Difference Time-Domain (FDTD) Method

The FDTD method, introduced by K. S. Yee in 1966, was the first direct time-domain technique for solution of Maxwell's differential (curl) equations on spatial grids or lattices (Yee 1966). The Yee algorithm solves both electric and magnetic fields in time and space by using the coupled Maxwell’s curl equations, rather than solving each independently wave equations. Maxwell’s curl equations are discretized in space and time by approximating with centered two-point finite differences (Taflove and Hagness 2005). There are several reasons for the expansion of interest in FDTD and related computational solution approaches for Maxwell's equations. The flexibility and capability of studying complex structures, easy implementation, visualizing the time-varying fields with the volume of space, handling nonlinear, frequency dependent, and conducting materials, obtaining easily broad spectral information by a single run made FDTD a powerful and

versatile numerical tool. The memory requirement is linearly proportional with the volume of the simulated structure (Kurt 2006). The FDTD method determines the frequency response over a wide spectrum of frequencies, whereas many other simulation methods require different models and/or techniques for different frequencies. As the FDTD method is time-based the results produced can also help us providing an insight to EM wave propagation within the structures. Results from FDTD simulations allow the wave to be visualized, which helps in checking results. Frequency-domain techniques often conceal how the EM waves propagate within the structure (Buchanan 1996).

3.1.1. Maxwell's Equations

For a region of space that has no electric or magnetic current sources, but may have materials that absorb electric or magnetic field energy, the time dependent Maxwell's equations are given in differential form (MKS units):

$$\frac{\partial \mathbf{B}}{\partial t} = -\nabla \times \mathbf{E} - \mathbf{M} \tag{3.1a}$$

$$\frac{\partial \mathbf{D}}{\partial t} = \nabla \times \mathbf{H} - \mathbf{J} \tag{3.1b}$$

$$\nabla \cdot \mathbf{D} = 0 \tag{3.1c}$$

$$\nabla \cdot \mathbf{B} = 0 \tag{3.1d}$$

where

B - magnetic flux density,

E - electric field,

M - equivalent magnetic current density,

D - electric flux density,

H - magnetic field,

J - electric current density.

In linear, isotropic, nondispersive materials we can apply the following simple relations:

$$\mathbf{D} = \varepsilon \mathbf{E} = \varepsilon_r \varepsilon_0 \mathbf{E} \quad , \quad \mathbf{B} = \mu \mathbf{H} = \mu_r \mu_0 \mathbf{H} \tag{3.2}$$

where

ε_0 - free-space permittivity,

ε_r - relative permittivity,

μ_0 - free-space permeability.

μ_r - relative permeability.

Here, $\mathbf{J}$ and $\mathbf{M}$ can act as independent sources of electric and magnetic fields energy, $\mathbf{J}_{source}$ and $\mathbf{M}_{source}$. Also, isotropic materials with nodispersive electric and magnetic losses are taken to study. This yield:

$$\mathbf{J} = \mathbf{J}_{source} + \sigma \mathbf{E} \quad , \quad \mathbf{M} = \mathbf{M}_{source} + \sigma^{*} \mathbf{H} \tag{3.3}$$

where σ is electric conductivity and σ^{*} is equivalent magnetic loss. By substituting equations (3.2), (3.3) into equations (3.1a), (3.1b) we obtain:

$$\frac{\partial \mathbf{H}}{\partial t} = -\frac{1}{\mu} \nabla \times \mathbf{E} - \frac{1}{\mu} \left(\mathbf{M}_{source} + \sigma^{*} \mathbf{H} \right) \tag{3.4}$$

$$\frac{\partial \mathbf{E}}{\partial t} = \frac{1}{\varepsilon} \nabla \times \mathbf{H} - \frac{1}{\varepsilon} \left(\mathbf{J}_{source} + \sigma \mathbf{E} \right) \tag{3.5}$$

The components of above equations in Cartesian coordinates are:

$$\begin{aligned}
\frac{\partial H_x}{\partial t} &= \frac{1}{\mu}\left[\frac{\partial E_y}{\partial z} - \frac{\partial E_z}{\partial y} - \left(M_{source_x} + \sigma^* H_x\right)\right] \\
\frac{\partial H_y}{\partial t} &= \frac{1}{\mu}\left[\frac{\partial E_z}{\partial x} - \frac{\partial E_x}{\partial z} - \left(M_{source_y} + \sigma^* H_y\right)\right] \\
\frac{\partial H_z}{\partial t} &= \frac{1}{\mu}\left[\frac{\partial E_x}{\partial y} - \frac{\partial E_y}{\partial x} - \left(M_{source_z} + \sigma^* H_z\right)\right]
\end{aligned} \tag{3.6}$$

$$\begin{aligned}
\frac{\partial E_x}{\partial t} &= \frac{1}{\varepsilon}\left[\frac{\partial H_z}{\partial y} - \frac{\partial H_y}{\partial z} - \left(J_{source_x} + \sigma E_x\right)\right] \\
\frac{\partial E_y}{\partial t} &= \frac{1}{\varepsilon}\left[\frac{\partial H_x}{\partial z} - \frac{\partial H_z}{\partial x} - \left(J_{source_y} + \sigma E_y\right)\right] \\
\frac{\partial E_z}{\partial t} &= \frac{1}{\varepsilon}\left[\frac{\partial H_y}{\partial x} - \frac{\partial H_x}{\partial y} - \left(J_{source_z} + \sigma E_z\right)\right]
\end{aligned} \tag{3.7}$$

The above six coupled partial differential equations form the basis of the FDTD method for electromagnetic wave interactions with objects in three dimensions (Taflove 1975).

3.2. General Formulation of FDTD Method

In 1966, Kane S. Yee introduced a set of finite-difference equations for the equations (3.6), (3.7) for the lossless materials case $\sigma = 0$ and $\sigma^* = 0$ (Taflove 2005). The adapted notation to represent a space point in a uniform, rectangular lattice is $(i, j, k) = (i\Delta x, j\Delta y, k\Delta z)$ where, Δx , Δy and Δz are the lattice increments in the Cartesian coordinates (Yee cell dimensions) and i , j and k are integers (Yee cell indices). The Yee unit cell and cell dimensions have been showed in Figure 3.1 schematically. Assume u is a function of space and time

$u = u(x, y, z, t)$. At a discrete point in the grid and at a discrete point in time the function can be written as:

$$u(i\Delta x, j\Delta y, k\Delta z, n\Delta t) = u\big|^{n}_{i,j,k} \tag{3.8}$$

where Δt is the time increment (time-step size) and n is an integer (time step index).The superscript n is related to time t by the equation $t = n\Delta t$. The space and time derivatives are approximated by centered two-point finite differences with second order accuracy

$$\frac{\partial u(i\Delta x, j\Delta y, k\Delta z, n\Delta t)}{\partial x} = \frac{u^{n}_{i+1/2,j,k} - u^{n}_{i-1/2,j,k}}{\Delta x} + O\left[(\Delta x)^2\right] \tag{3.9}$$

$$\frac{\partial u(i\Delta x, j\Delta y, k\Delta z, n\Delta t)}{\partial t} = \frac{u^{n+1/2}_{i,j,k} - u^{n-1/2}_{i,j,k}}{\Delta t} + O\left[(\Delta t)^2\right] \tag{3.10}$$

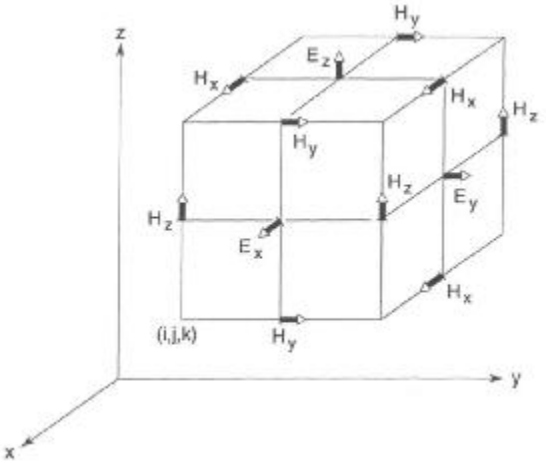

Figure 3.1. Cubic unit cell of the Yee space lattice, the electric and magnetic field vectors, and lattice increments (Taflove, 2005).

By applying the above notations, we can achieve a numerical approximation for the first equation of equation sets (3.7)

$$\frac{E_x\big|_{i,j+1/2,k+1/2}^{n+1/2} - E_x\big|_{i,j+1/2,k+1/2}^{n-1/2}}{\Delta t} = \frac{1}{\varepsilon_{i,j+1/2,k+1/2}}\left(\frac{H_z\big|_{i,j+1,k+1/2}^{n} - H_z\big|_{i,j,k+1/2}^{n}}{\Delta y} - \frac{H_y\big|_{i,j+1/2,k+1}^{n} - H_y\big|_{i,j+1/2,k}^{n}}{\Delta z} - J_{source_x}\big|_{i,j+1/2,k+1/2}^{n} - \sigma_{i,j+1/2,k+1/2} E_x\big|_{i,j+1/2,k+1/2}^{n}\right) \tag{3.11}$$

On the right-hand side of this equation, the magnetic field quantities are evaluated at time-step n, but the electric field and material conductivity values on the time-step n are not available. Because, only the previous values, $n-1/2$, of E_x are stored in the memory. The Figure 3.2 shows time-step Leap-Frogging in Yee algorithm. Here, the electric field values are defined at half time steps and magnetic field values are defined at whole number time steps. For adapting the time-step indices in equation (3.11) we use the well known semi-implicit approximation relation

$$E_x\big|_{i,j+1/2,k+1/2}^{n} = \frac{E_x\big|_{i,j+1/2,k+1/2}^{n+1/2} - E_x\big|_{i,j+1/2,k+1/2}^{n-1/2}}{2} \tag{3.12}$$

By substituting the equation (3.12) into equation (3.11), collecting all common terms, isolating $E_x^{n+1/2}$ on the left-hand side, and doing needed arithmetic calculations we can introduce an explicit form of finite-difference equation for E_x

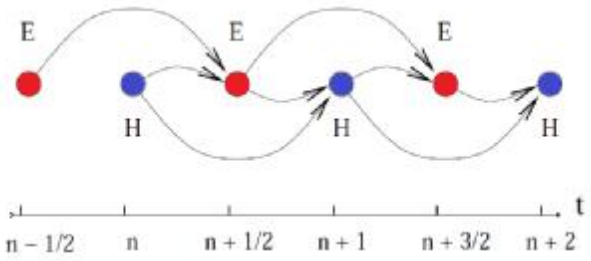

Figure 3.2. Time step leap-frogging in Yee algorithm.

$$E_x\big|_{i,j+1/2,k+1/2}^{n+1/2} = C_{a,E_x}\big|_{i,j+1/2,k+1/2} E_x\big|_{i,j+1/2,k+1/2}^{n-1/2} + C_{b,E_x}\big|_{i,j+1/2,k+1/2} \Big(H_z\big|_{i,j+1,k+1/2}^{n} - H_z\big|_{i,j,k+1/2}^{n} + H_y\big|_{i,j+1/2,k}^{n} - H_y\big|_{i,j+1/2,k+1}^{n} - J_{source}\big|_{i,j+1/2,k+1/2}^{n} \Big) \quad (3.13a)$$

By analogy, we can derive finite-difference equations for the rest of equations (3.7) and equations (3.6).

$$E_y\big|_{i-1/2,j+1,k+1/2}^{n+1/2} = C_{a,E_y}\big|_{i-1/2,j+1,k+1/2} E_y\big|_{i-1/2,j+1,k+1/2}^{n-1/2} + C_{b,E_y}\big|_{i-1/2,j+1,k+1/2} \Big(H_x\big|_{i-1/2,j+1,k+1}^{n} - H_x\big|_{i-1/2,j+1,k}^{n} + H_z\big|_{i-1,j+1,k+1/2}^{n} - H_z\big|_{i,j+1,k+1/2}^{n} - J_{source}\big|_{i-1/2,j+1,k+1/2}^{n} \Big) \quad (3.13b)$$

$$E_z\big|_{i-1/2,j+1/2,k+1}^{n+1/2} = C_{a,E_z}\big|_{i-1/2,j+1/2,k+1} E_z\big|_{i-1/2,j+1/2,k+1}^{n-1/2} + C_{b,E_z}\big|_{i-1/2,j+1/2,k+1} \Big(H_y\big|_{i,j+1/2,k+1}^{n} - H_y\big|_{i-1,j+1/2,k+1}^{n} + H_x\big|_{i-1/2,j,k+1}^{n} - H_x\big|_{i-1/2,j+1,k+1}^{n} - J_{source}\big|_{i-1/2,j+1/2,k+1}^{n} \Big) \quad (3.13c)$$

$$H_x\big|_{i-1/2,j+1,k+1}^{n+1} = D_{a,H_x}\big|_{i-1/2,j+1,k+1} H_x\big|_{i-1/2,j+1,k+1}^{n} + D_{b,H_x}\big|_{i-1/2,j+1,k+1} \Big(E_y\big|_{i-1/2,j+1,k+3/2}^{n+1/2} - E_y\big|_{i-1/2,j+1,k+1/2}^{n+1/2} + E_z\big|_{i-1/2,j+1/2,k+1}^{n+1/2} - E_z\big|_{i-1/2,j+3/2,k+1}^{n+1/2} - M_{source}\big|_{i-1/2,j+1,k+1}^{n+1/2} \Big) \quad (3.14a)$$

$$H_y\Big|_{i,j+1/2,k+1}^{n+1} = D_{a,H_y}\Big|_{i,j+1/2,k+1} H_y\Big|_{i,j+1/2,k+1}^{n} + D_{b,H_y}\Big|_{i,j+1/2,k+1} \Big(E_z\Big|_{i+1/2,j+1/2,k+1}^{n+1/2} - E_z\Big|_{i-1/2,j+1/2,k+1}^{n+1/2} + E_x\Big|_{i,j+1/2,k+1/2}^{n+1/2} - E_x\Big|_{i,j+1/2,k+3/2}^{n+1/2} - M_{source}\Big|_{i,j+1/2,k+1}^{n+1/2} \Delta\Big) \quad (3.14b)$$

$$H_z\Big|_{i,j+1,k+1/2}^{n+1} = D_{a,H_z}\Big|_{i,j+1,k+1/2} H_z\Big|_{i,j+1,k+1/2}^{n} + D_{b,H_z}\Big|_{i,j+1,k+1/2} \Big(E_x\Big|_{i,j+3/2,k+1/2}^{n+1/2} - E_x\Big|_{i,j+1/2,k+1/2}^{n+1/2} + E_y\Big|_{i-1/2,j+1,k+1/2}^{n+1/2} - E_y\Big|_{i+1/2,j+1,k+1/2}^{n+1/2} - M_{source}\Big|_{i,j+1,k+1/2}^{n+1/2} \Delta\Big) \quad (3.14c)$$

For cubic lattice $\Delta x = \Delta y = \Delta z = \Delta$ and updating coefficients C and D are defined as

$$C_a\Big|_{i,j,k} = \left(1 - \frac{\sigma_{i,j,k}\Delta t}{2\varepsilon_{i,j,k}}\right) \Big/ \left(1 + \frac{\sigma_{i,j,k}\Delta t}{2\varepsilon_{i,j,k}}\right), \quad C_b\Big|_{i,j,k} = \left(\frac{\Delta t}{\varepsilon_{i,j,k}\Delta}\right) \Big/ \left(1 + \frac{\sigma_{i,j,k}\Delta t}{2\varepsilon_{i,j,k}}\right) \quad (3.15)$$

$$D_a\Big|_{i,j,k} = \left(1 - \frac{\sigma^*_{i,j,k}\Delta t}{2\mu_{i,j,k}}\right) \Big/ \left(1 + \frac{\sigma^*_{i,j,k}\Delta t}{2\mu_{i,j,k}}\right), \qquad D_b\Big|_{i,j,k} = \left(\frac{\Delta t}{\mu_{i,j,k}\Delta}\right) \Big/ \left(1 + \frac{\sigma^*_{i,j,k}\Delta t}{2\mu_{i,j,k}}\right) \quad (3.16)$$

Equations (3.13), (3.14) are the general form of finite-difference expressions of equations (3.4), (3.5) and are known as the three dimensional (3D) FDTD method equations. It is clear from these equations, the electric field values are only defined at half time steps and the magnetic field values are only defined at whole ones. This allows electric and magnetic field components updates in a FDTD analysis to be interlaced in time. Electric field values are calculated at each time step, and then the magnetic field values are calculated at next time step. As shown in Figure 3.2 for updating a field component, only past electric and magnetic field components are required (Hill 1996). Of course, at the beginning the initial conditions are needed as all EM problems.

The equations (3.13), (3.14) have been driven regardless to the medium are studying. Simplifications can be applied as following sections.

3.3. Maxwell's Equations in Isotropic Medium

The time-dependent Maxwell's curl equations in isotropic medium ($\varepsilon = \varepsilon_0 \varepsilon_r$, $\mu = \mu_r \mu_0$ and $\mu_r = 1$) are

$$\frac{\partial \mathbf{E}}{\partial t} = \frac{1}{\varepsilon_0 \varepsilon_r} \nabla \times \mathbf{H} \tag{3.17}$$

$$\frac{\partial \mathbf{H}}{\partial t} = -\frac{1}{\mu_0} \nabla \times \mathbf{E} \tag{3.18}$$

The components of above equations in Cartesian coordinates are:

$$\begin{aligned}
\frac{\partial E_x}{\partial t} &= \frac{1}{\varepsilon_0 \varepsilon_r}\left(\frac{\partial H_z}{\partial y} - \frac{\partial H_y}{\partial z}\right) \\
\frac{\partial E_y}{\partial t} &= \frac{1}{\varepsilon_0 \varepsilon_r}\left(\frac{\partial H_x}{\partial z} - \frac{\partial H_z}{\partial x}\right) \\
\frac{\partial E_z}{\partial t} &= \frac{1}{\varepsilon_0 \varepsilon_r}\left(\frac{\partial H_y}{\partial x} - \frac{\partial H_x}{\partial y}\right)
\end{aligned} \tag{3.19}$$

$$\begin{aligned}
\frac{\partial H_x}{\partial t} &= \frac{1}{\mu_0}\left(\frac{\partial E_y}{\partial z} - \frac{\partial E_z}{\partial y}\right) \\
\frac{\partial H_y}{\partial t} &= \frac{1}{\mu_0}\left(\frac{\partial E_z}{\partial x} - \frac{\partial E_x}{\partial z}\right) \\
\frac{\partial H_z}{\partial t} &= \frac{1}{\mu_0}\left(\frac{\partial E_x}{\partial y} - \frac{\partial E_y}{\partial x}\right)
\end{aligned} \tag{3.20}$$

3.4. One Dimensional FDTD

For one dimensional propagation, we can assume: a) $E_x \neq 0$, $E_y = 0$ and $E_z = 0$. b) There isn't any variation in the x- y surface ($\frac{\partial}{\partial x} = 0$ and $\frac{\partial}{\partial y} = 0$). So the equations (3.19), (3.20) reduce to the following equations:

$$\frac{\partial H_x}{\partial t} = \frac{1}{\mu_0}\left(\frac{\partial E_y}{\partial z} - \frac{\partial E_z}{\partial y}\right) = 0 \tag{3.21}$$

$$\frac{\partial H_y}{\partial t} = \frac{1}{\mu_0}\left(\frac{\partial E_z}{\partial x} - \frac{\partial E_x}{\partial z}\right) = -\frac{1}{\mu_0}\frac{\partial E_x}{\partial z} \tag{3.22}$$

$$\frac{\partial H_z}{\partial t} = \frac{1}{\mu_0}\left(\frac{\partial E_x}{\partial y} - \frac{\partial E_y}{\partial x}\right) = 0 \tag{3.23}$$

$$\frac{\partial E_x}{\partial t} = \frac{1}{\varepsilon_0\varepsilon_r}\left(\frac{\partial H_z}{\partial y} - \frac{\partial H_y}{\partial z}\right) = -\frac{1}{\varepsilon_0\varepsilon_r}\frac{\partial H_y}{\partial z} \tag{3.24}$$

In addition, if the propagation of 1D EM wave be in z direction and electric field is x –polarized ($H_x = H_z = 0$), then Maxwell's equations can be written as

$$\frac{\partial E_x}{\partial t} = -\frac{1}{\varepsilon_0\varepsilon_r}\frac{\partial H_y}{\partial z} \tag{3.25}$$

$$\frac{\partial H_y}{\partial t} = -\frac{1}{\mu_0}\frac{\partial E_x}{\partial z} \tag{3.26}$$

These equations are used in simulation of wave propagation in one dimension. In FDTD formulation, by using the central difference approximation in both the spatial and time derivatives we can express the equation (3.25) at space-time point $(z = k\Delta z, t = n\Delta t)$ as

$$\frac{E_x\big|_k^{n+1/2} - E_x\big|_k^{n-1/2}}{\Delta t} = -\frac{1}{\varepsilon_0\varepsilon_r}\frac{H_y\big|_{k+1/2}^{n} - H_y\big|_{k-1/2}^{n}}{\Delta z} \tag{3.27}$$

Similarly, the equation (3.26) can be written at time-space point $(z + \Delta z/2, t + \Delta t/2)$ as

$$\frac{H_y\big|_{k+1/2}^{n+1} - H_y\big|_{k+1/2}^{n}}{\Delta t} = -\frac{1}{\mu_0}\frac{E_x\big|_{k+1}^{n+1/2} - E_x\big|_{k}^{n+1/2}}{\Delta z} \tag{3.28}$$

Solving for E_x and H_y at time step $n+1/2$ and $n+1$ respectively yields

$$E_x\big|_k^{n+1/2} = E_x\big|_k^{n-1/2} - \frac{\Delta t}{\varepsilon_0\varepsilon_r \Delta z}\left(H_y\big|_{k+1/2}^{n} - H_y\big|_{k-1/2}^{n}\right) \tag{3.29}$$

$$H_y\big|_{k+1/2}^{n+1} = H_y\big|_{k+1/2}^{n} - \frac{\Delta t}{\mu_0 \Delta z}\left(E_x\big|_{k+1}^{n+1/2} - E_x\big|_{k}^{n+1/2}\right) \tag{3.30}$$

As mentioned in the section 3.2, this system of equations is coupled or interlocked. If a source is defined at some places in the computational domain,

propagation of light from this source in time and space can be obtained starting from equation (3.29) by inserting some initial values of fields corresponding to this source. Then electric field at the next time step might be evaluated straightforwardly and if inserted to equation (3.30) magnetic field components in the next time step can also be found. This time staggered calculation of electric and magnetic field components is often called leapfrogging. Proceeding the time cycle gives evolution of fields in time and space which was searched for. In Figure 3.3 each row corresponds to a specific instant in time, at half time steps, whereas each column represents a single spatial grid point through time. The gray and blue grid lines represent whole and half steps respectively, in both time and space. The orange triangles represent E_x while the purple triangles represent H_y. We see that for every triangle there are three arrows pointing towards it. One comes from the previous time step. The other two come from a half-step down and a half-step to the right or left. The initial values that must be given are the green circles, and the boundaries are the orange and purple circles.

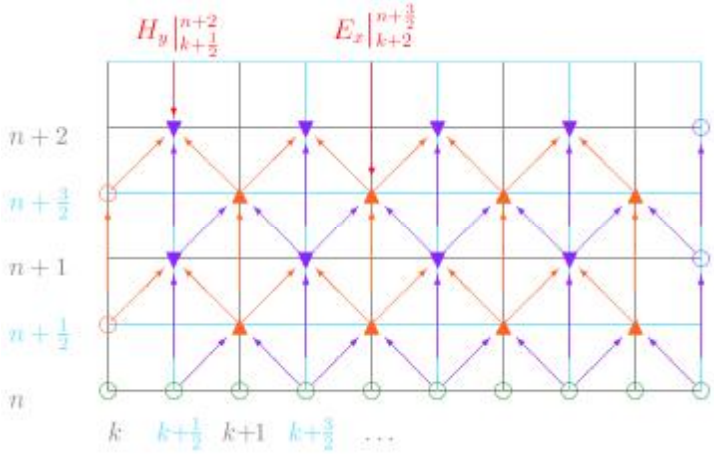

Figure 3.3. The FDTD approximation grid.

The magnitudes of Equations (3.25) and (3.26) are not the same degree because $\mu_0/\varepsilon_0 \approx 1.4 \times 10^5$. We want them to be for our computations. So, a change of variables is necessary to fix this discrepancy in our equations. By substituting $\tilde{E}_x = \sqrt{\varepsilon_0/\mu_0}\, E_x$ in Equations (3.29) and (3.30) we have

$$\tilde{E}_x\Big|_k^{n+1/2} = \tilde{E}_x\Big|_k^{n-1/2} - \frac{1}{\varepsilon_r\sqrt{\varepsilon_0\mu_0}}\frac{\Delta t}{\Delta z}\left(H_y\Big|_{k+1/2}^{n} - H_y\Big|_{k-1/2}^{n}\right) \tag{3.31}$$

$$H_y\Big|_{k+1/2}^{n+1} = H_y\Big|_{k+1/2}^{n} - \frac{1}{\sqrt{\varepsilon_0\mu_0}}\frac{\Delta t}{\Delta z}\left(\tilde{E}_x\Big|_{k+1}^{n+1/2} - \tilde{E}_x\Big|_{k}^{n+1/2}\right) \tag{3.32}$$

Now, we have a discrete representation of 1D FDTD in general form. By considering the stability of algorithm, initial values and boundary condition the suitable codes can be written in desired programming language.

3.4.1. Stability of FDTD Algorithm

The choice of space increment and time-step can affect the performance (stability and the accuracy) of the finite-difference approximations to Maxwell's differential equations. For example in 1D simulation, an EM wave requires a minimum time of $\Delta t = \Delta x / c_0$ to propagate a distance of one cell Δx in free space. It is arises from the fact that an electromagnetic wave cannot propagate faster than the speed of light in free space. When we get to 2D simulation, we have to allow for the propagation in the diagonal direction, which brings the time to $\Delta t = \Delta x/(\sqrt{2}c_0)$. Obviously, 3D simulation requires $\Delta t = \Delta x/(\sqrt{3}c_0)$ (Sullivan, 2000). Generally, the Courant number or numerical stability factor defined as

$$S = \frac{c\Delta t}{\sqrt{\Delta x^2 + \Delta y^2 + \Delta z^2}} \tag{3.33}$$

For the stability of FDTD algorithm $S \leq 1$ must be satisfied. This stability criterion ensures the convergence of the numerical simulation. The cell size Δx should sample adequate portion of the minimum wavelength component (worst scenario case) of the EM field. Usually $\Delta x \leq \lambda_{min} / 20$ is safe for enough accuracy but depending on the situation one may increase or reduce the sampling rate. As the pulse propagates down the FDTD mesh, the pulse becomes distorted (broadening and ringing the tail of the pulse) due to the numerical dispersion. Well resolved grid resolution also enables solution which is independent of the angle of the propagation (Kurt 2006).

3.4.2. Boundary Conditions

One of the major problems with any beam propagation method is that the computational region has to be truncated by numerical boundaries. The numerical boundary is represented by the extreme points on which the field is sampled. Because the whole numerical scheme is generally lossless, the total energy within the computational region remains the same, and hence any wave that in reality should leave this region is directed back into it, thereby representing an unreal phenomenon. The conventional way to reduce the effect of this problem is to put a strongly absorbing medium of appropriate thickness at the edge of the computational region, thereby imposing the so-called absorbing boundary condition (ABC) (Agrawal 2004). They should absorb the out-going EM field by suppressing the spurious back reflected energy regardless of the polarization, propagation direction, and frequency. ABC, perfectly matched layer (PML), or periodic boundary condition (PBC) are usually implemented with FDTD.

3.4.2.1. Perfectly Matched Layer (PML)

The main problem with FDTD method and any beam propagation method is that the simulation region has to be represented by a finite domain bounded by numerical boundaries. Because the whole numerical scheme is generally lossless, the total energy within the numerical region remains the same, and hence any wave that should leave the region is directed back into it, thereby representing an unreal phenomenon. The conventional way to reduce the effect of this problem is to put a strongly absorbing medium of appropriate thickness at the edge of the region, thereby imposing the so-called absorbing boundary condition (Agrawal and Sharma 2004). The most used boundary condition in FDTD method is perfectly matched layer (PML). PML is an absorbing medium that is commonly used to truncate numerical simulations of electromagnetism and other wave equations in FDTD simulations. Actually, it is powerful technique to absorb waves incident on the boundaries of wave-equation simulation. The layer has reflectionless property and interfaces between the simulation region and adjacent media. The concept of PML was introduced by Berenger (Berenger 1994) for application of FDTD solutions for Maxwell's equations. In the PML method a layer of a specially designed anisotropic medium is put at the edge of the simulation region as have been showed in Figure 3.4. The absorption profile in this layer can be arbitrarily chosen, subject to certain conditions. The PML boundary condition was found to be highly effective for applications to optical wave propagation and have been developed to different version (Agrawal and Sharma 2004).

3.5. Two Dimensional FDTD

In this study all the simulations have been done in two dimensions. So, after introducing the general formulation of FDTD method in three dimension and presentation related parameters in one dimension we turn the discussion to two dimension FDTD. We can assume the structure being studied extends to infinity in the in the z-direction without any changes in the transverse cross section. If the

incident wave is also uniform in the z-direction, all the partial derivations of the fields with respect to z will be zero in Equations (3.19) and (3.20). So these equation reduces to:

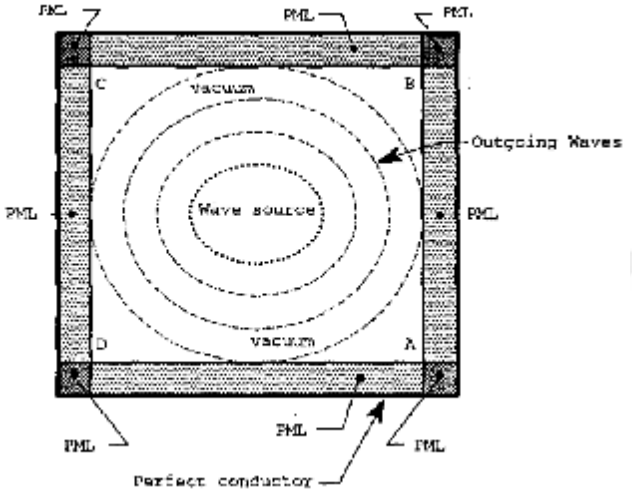

Figure 3.4. Schematic of perfectly matched layer (PML) (Berenger 1994).

$$\begin{aligned}
\frac{\partial E_x}{\partial t} &= \frac{1}{\varepsilon_0 \varepsilon_r}\frac{\partial H_z}{\partial y} \\
\frac{\partial E_y}{\partial t} &= \frac{1}{\varepsilon_0 \varepsilon_r}\left(-\frac{\partial H_z}{\partial x}\right) \\
\frac{\partial E_z}{\partial t} &= \frac{1}{\varepsilon_0 \varepsilon_r}\left(\frac{\partial H_y}{\partial x} - \frac{\partial H_x}{\partial y}\right)
\end{aligned} \tag{3.34}$$

$$\begin{aligned}
\frac{\partial H_x}{\partial t} &= \frac{1}{\mu_0}\left(-\frac{\partial E_z}{\partial y}\right) \\
\frac{\partial H_y}{\partial t} &= \frac{1}{\mu_0}\left(\frac{\partial E_z}{\partial x}\right) \\
\frac{\partial H_z}{\partial t} &= \frac{1}{\mu_0}\left(\frac{\partial E_x}{\partial y} - \frac{\partial E_y}{\partial x}\right)
\end{aligned} \tag{3.35}$$

In general form of 2D FDTD formulation, we choose between one of the two groups of three electromagnetic fields components.

1) The transverse electric (TE) mode, which is composed of E_x, E_y and H_z.
2) The transverse magnetic (TM) mode, which is composed of E_z, H_x and H_y.

The most important note here is that in the study of waveguides, as the simulation in the following chapters the TE and TM modes are defined as do in optics, but here we must continue the formulation in the general form of FDTD method. For TE mode we have the following set equations:

$$\begin{aligned}
\frac{\partial E_x}{\partial t} &= \frac{1}{\varepsilon_0 \varepsilon_r}\frac{\partial H_z}{\partial y} \\
\frac{\partial E_y}{\partial t} &= \frac{1}{\varepsilon_0 \varepsilon_r}\left(-\frac{\partial H_z}{\partial x}\right) \\
\frac{\partial H_z}{\partial t} &= \frac{1}{\mu_0}\left(\frac{\partial E_x}{\partial y} - \frac{\partial E_y}{\partial x}\right)
\end{aligned} \tag{3.36}$$

and TM mode include the equations:

$$\begin{aligned}
\frac{\partial E_z}{\partial t} &= \frac{1}{\varepsilon_0 \varepsilon_r}\left(\frac{\partial H_y}{\partial x} - \frac{\partial H_x}{\partial y}\right) \\
\frac{\partial H_x}{\partial t} &= -\frac{1}{\mu_0}\frac{\partial E_z}{\partial y} \\
\frac{\partial H_y}{\partial t} &= \frac{1}{\mu_0}\frac{\partial E_z}{\partial x}
\end{aligned} \tag{3.37}$$

These two modes constitute the two possible ways that 2D FDTD problems can be set up for the case of zero partial derivation in the z-direction. As can be seen the TE and TM modes contain no common field components. So, these modes can sexist simultaneously with no mutual interaction for structures composed of isotropic materials or anisotropic materials having no off-diagonal components in the constitutive tensors (Taflove and Hagness 2005).

3.6. Maxwell's fish-eye (MFE)

The main structure that has been studied in this thesis, especially in units 4 and 5 is Maxwell's fish-eye as a graded index (GRIN) medium. The original MFE is an unbounded, spherically symmetric, inhomogeneous medium which is infinitely large (Luneburg 1964). In this work, the bounded form of MFE with a perfectly electrical conductor boundary (Leonhardt 2009, Liu et al 2013) will be used. The refractive index of bounded MFE varies according to a reverse quadratic function of distance $n(r) = n_0 / 1 + (r / R)^2$, where n_0 is the refractive index in the origin, R is the physical radius of MFE, and the radius r is measured in spherical coordinate system (Liu et al 2013). As has been showed in the Figure 3.5 the refractive index in the center of MFE, n_0 , reduces uniformly to $n_0 / 2$ in the edge of disc. Here we assume the refractive index of MFE in the center is 3.4641 accordance to next units' simulations.

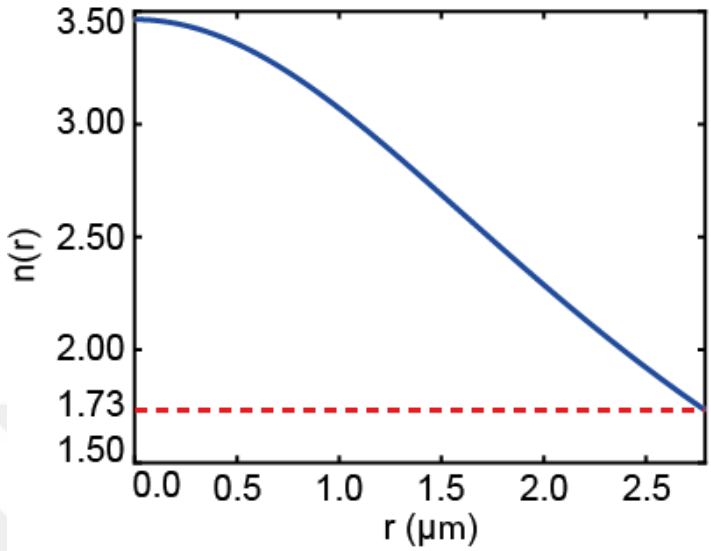

Figure 3.5. Refractive index of Maxwell's fish-eye for $n_0 = 3.4641$ and $R = 2.79\,mm$.

3.7. Important Design Parameters of Microresonators

In this section, we briefly introduce and derive simple expressions for parameters that are important in realization of microresonators. Calculation of the Q-factor is the most important computational tasks in investigation of light behavior in resonators. The Q-factor is related to photon lifetime in microresonators. In other words, it is proportional to stored energy inside microresonators and inversely proportional to losses from microresonators. Bending loss, scattering loss and material loss are the main loss mechanisms for a microresonator (Rabiei, et al 2002). Bending loss is primarily determined by the index difference between resonator and surrounding medium. The familiar definition of the Q-factor is:

$$Q = \frac{w_0}{\Delta w}\,, \tag{3.38}$$

where w_0 is resonant frequency. Practically, the Q-factor of a resonator is defined by

$$Q = \frac{f_0}{\Delta f_{FWHM}} = \frac{\lambda_0}{\Delta \lambda_{FWHM}}, \tag{3.39}$$

where FWHM is full width of half maximum of related resonance, f_0 and λ_0 are frequency and wavelength of resonance respectively (Chremmos et al 2010).

The other important parameter that must be considered for studying of microresonators is free spectral range (FSR), which is basically the distance between the resonances in transmission spectrum of a microresonator. Simply the FSR are defined as:

$$FSR = f_{m+1} - f_m = \lambda_{m+1} - \lambda_m \tag{3.40}$$

Finally, another important parameter for measuring of resonator performance is finesse (ℱ). The finesse is defined and calculated (approximately) as (Rabiei, et al 2002, Chremmos et al 2010)

$$\mathcal{F} = \frac{FSR}{\Delta \lambda_{FWHM}} \tag{3.41}$$

This parameter and FSR are the most important parameters for a microresonator (Rabiei, et al 2002).

3.8. Computational Tools

In this thesis, in addition to analytical calculations, the computational finite-difference time-domain (FDTD) method has been used. We implemented the FDTD method by MEEP program and Lumerical commercial software.

The MEEP package is Linux based free software from MIT Nanostructures and Computation research group. This program computes definite-frequency eigenmodes of Maxwell's equations in periodic dielectric structures, especially for the photonic crystals, for arbitrary wavevectors, using fully-vectorial and three-dimensional methods. It is also applicable to many other problems in optics, such as waveguides and resonator systems.

Nowadays, some commercial FDTD software packages are available. We have useed the FDTD Solutions introduced by Lumerical Company (https://www.lumerical.com). FDTD Solutions is generally a windows based package. It is a 3D Maxwell Equations solver, capable of analyzing the interaction of electromagnetic waves with complicated structures employing wavelength scale features.

4. GRADED INDEX MICRORESONATORS[1]

4.1. Introduction

Whispering gallery modes (WGMs) in optical microresonators (or microcavities) have been studied vastly in the past two decades (Vahala 2003). WGMs are eigenmodes of wave field inside a given resonator with smooth edges. Theoretical and experimental studies have been conducted by several groups on WGMs in microresonators, and this is due to the spatial and temporal confinement of light in these structures. As a matter of course, these modes mainly depend on the geometry of resonator which is open to engineering possibilities. Optical WGM microresonators have led to many applications in various fields such as single photon sources in cavity quantum electrodynamics (QED) applications, interfaces for quantum communications, microlasers, biosensing, optical circuits, dynamic filters and switches in optical communications (Michler et al 2000, Wilk et al 2007, Sandoghdar et al 1996, Armani et al 2007, Franchimon et al 2013, Djordjev et al 2002). Concurrently, graded index (GRIN) structures have been receiving great interest in recent years. These structures are inhomogeneous media with spatially varying refractive index distributions. GRIN structures are widely used in optics and photonics applications due to their unique light coupling, focusing, modeling, and switching abilities (Gomez-Reino et al 2002).

Among GRIN structures, the Maxwell's fish eye (MFE) is of special interest and can be implemented using dielectric materials. The original MFE is an unbounded, spherically symmetric, inhomogeneous medium which is infinitely large (Luneburg 1964). Recently, the modified form of MFE is being investigated in literature and it is bounded with a perfectly electrical conductor boundary (Leonhardt 2009, Liu et al 2013). In this work, the bounded form of MFE will be

[1] This chapter is based on: Dadashi, Kh., Kurt, H., Ustun, K., Esen, R., 2014. Graded Index Optical Microresonators: Analytical and Numerical Analyses, J. Opt. Soc. Am. B, 31(9): 2239–2245.

used. The refractive index of bounded MFE varies according to a reverse quadratic function of distance (Liu et al 2013):

$$n(r) = \frac{n_0}{1+(r/R)^2}\ , \tag{4.1}$$

where n_0 is the refractive index in the origin, R is the physical radius of MFE, and the radius r is measured in spherical coordinate system, $r = (x^2 + y^2 + z^2)^{1/2}$.

In recent works on MFE, more attention has been paid to the imaging properties of MFE lens in the framework of wave optics. Achieving the perfect image and enhancing the resolution were the main objectives in studies of Leonhardt (2009) and Leonhardt and Philbin (2010). In another work, designing of a wide angle terahertz detectors with independent incident angle have been recently studied by Liu et al (2013).

The study of the MFE as a boundary value problem within the framework of Maxwell equations goes back to Tai (1958) works. Two second order differential equations for transverse electric (TE) and transverse magnetic (TM) modes were derived. Equations were changed to hypergeometric differential equation form but because of the lack of appropriate computing systems calculations of these equations were delayed for some years. Later, Rosu and Reyes (1984) computed the radial behavior of TE and TM modes based on the Tai's previously derived equations. They found analytical expressions for both TE and TM modes. The azimuthal modes were not mentioned in this work and only radial modes of solitary MFE were introduced.

Radially GRIN media with different profiles and various material types (metamaterials, plasmonics etc.) have been investigated for different applications. An omnidirectional photonic hole was proposed and the incident optical energy

was stored for a certain period of time by Liu et al (2010). Narimanov et al (2009) proposed an effective optical black hole that provides broad-band omnidirectional light absorption. In another study, gravitational lensing effects were demonstrated with a microstructure waveguide that was used as an omnidirectional absorber holding potential for light harvesting and microcavity applications (Sheng et al 2013). Efficient light transportation through a sharp waveguide corner was achieved by GRIN waveguide (Wang et al 2012). Hollow core fiber with a radially GRIN cladding was studied to increase the light penetration towards the core region by Zhu et al (2012). Plasmonic Luneburg and Eaton lenses were investigated to focus and bend surface plasmon polaritons (Zentgraf et al 2011). In that work, scattering losses were reduced due to gradual change of the optical properties. From this quick literature review, we can claim that there is a growing interest to propose and investigate more complex and advanced photonic materials for manipulating light interaction with the designed structures.

This chapter of the present thesis provides the solution for the eigenvalue problem associated with the radially inhomogeneous disc resonator. The near-field maps of higher order WGMs of the MFE disc resonator are extracted. The main task of this chapter is to derive analytical and numerical solution to the specific problem at hand. Then, MFE resonators as building blocks for integrated photonic circuits will be explored paying attention to different aspects such as Q-factors, free-spectral range, and scattering losses.

In this chapter, we introduce the idea of combining optical microdisc with GRIN medium that is represented by 2D MFE. The optical resonant modes of the structure are calculated both analytically and numerically. The analytical solution for planar disc with step index contrast can be found in the literature (Quan and Guo, 2009). The analytical solution together with finite-difference time-domain (FDTD) exploration of MFE microresonator are proposed in this chapter for the first time to the best of our knowledge.

As mentioned before, attempts to find the electromagnetic modes of MFE resonator can be found in Tai (1958) and Rosu and Reyes (1994). The formulations in these studies were carried out in terms of a boundary-value problem and general discussion involving a radially stratified medium was adapted. Rosu and Reyes (1994) ended up with the same type of solution as ours but following a rather different approach. It could be important to have an alternative derivation for the same problem with detailed explanation of the intermediate steps. Besides, extraction of the supported modes in an alternative and complementary way via FDTD was carried out in this chapter.

4.2. Maxwell's Fish Eye as Graded Index Microresonator

To analyze the behavior of MFE microresonator, we use Helmholtz equation for TE modes. In general, one should be careful while attempting to drive the Helmholtz equation starting from the Maxwell equations if the medium has inhomogeneous refractive index profile $\varepsilon(r)$. In our case due to spatial form of $\varepsilon(r)$, we have the second order differential equation which is the same as general Helmholtz equation that can be derived for an homogenous medium.

4.2.1. Helmholtz Equation

In a GRIN structure where the refractive index $n(r)$ is only a function of the radial parameter r measured from the origin of the coordinate system, the Maxwell equations in nonmagnetic source-free region can be written as follows:

$$\nabla \times \mathbf{E} = i\omega\mu_0\mathbf{H} \tag{4.2a}$$

$$\nabla \times \mathbf{H} = -i\omega\varepsilon_0\varepsilon(r)\mathbf{E} \tag{4.2b}$$

$$\nabla \cdot [\varepsilon(r)\mathbf{E}] = 0 \tag{4.2c}$$

$$\nabla \cdot \mathbf{H} = 0 \tag{4.2d}$$

In these equations, it was assumed that the electromagnetic fields have time dependence in the form of $\exp(-i\omega t)$ where ω is angular frequency, ε_0 and μ_0 are permittivity and permeability of free space, $\varepsilon(r)$ denotes the permittivity of the media as mentioned before and we assume $\mu(r) = 1$ as is usual for most materials. Starting with equation (4.2a) we have:

$$\nabla \times \nabla \times \mathbf{E} - k^2 \varepsilon(r)\mathbf{E} = 0, \tag{4.3}$$

where $k = \omega / c = (2\pi / \lambda_0)$ is wave number in free space. Equation (4.3) can be rewritten as:

$$\nabla(\nabla \cdot \mathbf{E}) - \nabla^2 \mathbf{E} - k^2 \varepsilon(r)\mathbf{E} = 0. \tag{4.4}$$

One can easily show that for the present problem at hand under the transverse electric (TE) mode case, the first term of equation (4.4) can be discarded. When we evaluate equation (4.2c):

$$[\nabla \varepsilon(r)] \cdot \mathbf{E} + \varepsilon(r)\nabla \cdot \mathbf{E} = 0. \tag{4.5}$$

The first term of last equation can be extracted in spherical coordinates as:

$$[\nabla \varepsilon(r)] \times \mathbf{E} = \frac{\partial \varepsilon(r)}{\partial r} E_r + \frac{\partial \varepsilon(r)}{r \partial \theta} E_\theta + \frac{\partial \varepsilon(r)}{r \sin\theta \, \partial \phi} E_\phi . \tag{4.6}$$

For TE modes, **E** doesn't have any component in the x-y plane so $E_r = 0$. As a result the first term of equation (4.6) becomes zero. On the other

hand, $\varepsilon(r)$ is homogeneous in θ and ϕ so the other two terms of equation (4.6) turn out to zero as well. Consequently, $[\nabla\varepsilon(r)]\cdot\mathbf{E}=0$. It can be concluded from equation (4.5) that $\nabla\cdot\mathbf{E}=0$ and the form given in equation (4.4) transform into the Helmholtz equation for TE modes as follows:

$$\nabla^2\mathbf{E}+k^2\varepsilon(r)\mathbf{E}=0. \tag{4.7}$$

where $k=\omega\sqrt{\varepsilon_0\mu_0}=\omega/c$, $k=(2\pi/\lambda_0)$ is wave number, λ_0 wave length, c speed of light, ε_0 permittivity and μ_0 is permeability of the free space. ω is angular frequency and $\varepsilon(r)=n(r)^2$ is permittivity of the media and as is usual for most materials we assumed $\mu(r)=1$.

4.3. Analytical Solutions of Helmholtz Equation

Two dimensional representation of Maxwell's fish eye as a GRIN medium is shown in Figure 4.1(a). In Figure 4.1(b) a 3D representation of refractive index distribution of the complete configuration is shown. For TE - polarized waves that propagate in the x - y plane, the E-field has only the z component. So, the equation (4.7) can be expressed as follow in the 2D polar coordinates:

$$\frac{\partial^2 E_z}{\partial r^2}+\frac{1}{r}\frac{\partial E_z}{\partial r}+\frac{1}{r^2}\frac{\partial^2 E_z}{\partial\varphi^2}+k^2\varepsilon(r)E_z=0. \tag{4.8}$$

To solve equation (4.8) we assume the separation of variables in the form of:

$$E_z(r,\varphi)=\Psi(r)\Phi(\varphi), \tag{4.9}$$

and introduce the separation constant m. As a result, the equation (4.8) can be separated as follows:

$$\frac{d^2\Phi(\varphi)}{d\varphi^2} + m^2\Phi(\varphi) = 0, \tag{4.10a}$$

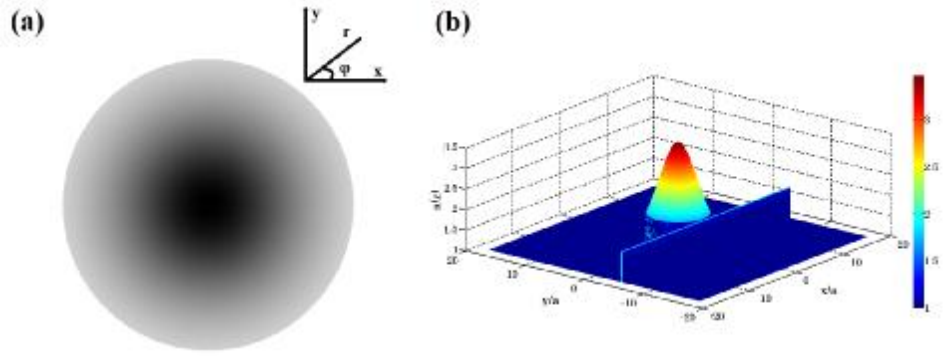

Figure 4.1. (a) Schematic view of 2D Maxwell's fish eye. (b) The 3D representation of refractive index distribution of the complete configuration including bus waveguide and MFE resonator.

$$\frac{d^2\Psi(r)}{dr^2} + \frac{1}{r}\frac{d\Psi(r)}{dr} + \left[\frac{k^2 n_0^{\,2}}{[1+(r/R)^2]^2} - \frac{m^2}{r^2}\right]\Psi(r) = 0 \qquad r \le R, \tag{4.10b}$$

$$\frac{d^2\Psi(r)}{dr^2} + \frac{1}{r}\frac{d\Psi(r)}{dr} + \left[k^2 - \frac{m^2}{r^2}\right]\Psi(r) = 0 \qquad r > R. \tag{4.10c}$$

Equations (4.10b) and (4.10c) are valid for the inside and outside of the MFE disc, respectively.

The general solutions of equation (4.10a) are in the form of:

$$\Phi_m(\varphi) = \sum_m \left(A_m \cos m\varphi + B_m \sin m\varphi\right) \qquad m = 1,2,3..., \tag{4.11}$$

where A_m, B_m are constants and m will be the azimuthal mode number. Due to symmetry of the system, B_m will be omitted. Then, the solutions can be written in a simple and compact form as:

$$F_m(\varphi) = \sum_m A_m \cos m\varphi \qquad m = 1,2,3.... \tag{4.12}$$

For analytical solution of equations (4.10b) and (4.10c) we change the radial variable to $x = r/R$ and introduce the constant $\eta = (1 - (1 + k_0^2 n_0^2 R^2)^{1/2})/2$. After that, the general solutions can be written as:

$$\begin{aligned} \Psi_m^{in}(x) = \sum_m \{ & C_m^+ R^{m+2\eta} x^m (1+x^2)^\eta F([\eta, \eta+m], [m+1], -x^2) \\ & + C_m^- R^{-m+2\eta} x^{-m} (1+x^2)^\eta F([\eta, \eta-m], [-m+1], -x^2) \}, \end{aligned} \tag{4.13}$$

where C_m^+, C_m^- are real constants and F is hypergeometric function (Arfken and Weber, 2005). C_m^- must vanish because the second term in equation (4.13) have singularity in the origin. The solutions for equation (4.10c) are in the form of $\Psi_m^{out}(r) = real\{D_m H_m(kr)\}$ where D_m are complex constants and $H_m(kr)$ are the Hankel functions and are defined as $H_m(kr) = J_m(kr) \pm jY_m(kr)$, $j = \sqrt{-1}$. $J_m(kr)$ and $Y_m(kr)$ denote Bessel function of first and second kind (Arfken and Weber, 2005). As a result, we have the following solutions for $r \geq R$ region:

$$\Psi_m^{out}(r) = \sum_m real\{D_m(J_m(kr) \pm jY_m(kr))\}. \tag{4.14}$$

From the continuity condition of $\Psi_m(r)$ at the interface of MFE with the environment, $r = R$ or $x = 1$, the following equation is obtained:

$$C_m^+ R^{m+2\eta} 2^\eta F([\eta, \eta + m], [m+1], -1) = D_m (J_m(kR) \pm jY_m(kR)), \quad (4.15)$$

which correlates the amplitudes D_m to C_m^+:

$$D_m = \frac{C_m^+ R^{m+2\eta} 2^\eta F([\eta, \eta + m], [m+1], -1)}{(J_m(kR) \pm jY_m(kR))}. \quad (4.16)$$

By choosing the real part of the equation (4.14) and performing algebraic manipulations, the equation (4.9), can be written as in the following forms:

$$E_z^{in}(r,\varphi) \equiv E_z^{in}(x,\varphi) = \sum_m \{A_m C_m^+ R^{m+2\eta} x^m (1+x^2)^\eta F([\eta, \eta + m], [m+1], -x^2) \cos(m\varphi)\} \quad r \le R, \quad (4.17a)$$

$$E_z^{out}(r,\varphi) = \sum_m \{A_m C_m^+ R^{m+2\eta} 2^\eta F([\eta, \eta + m], [m+1], -1) \cdot \frac{(J_m(kR)J_m(kr) + Y_m(kR)Y_m(kr))}{(J_m^2(kR) + Y_m^2(kR))} \cos(m\varphi)\} \quad r \ge R. \quad (4.17b)$$

Continuity condition of the first order derivative of E_z (E_z^{in}, E_z^{out}) with respect to r (or equivalently x) at the interface of MFE ($r = R$ or $x = 1$) follows:

$$C_m^+ R^{m+2h} \times 2^h \times \frac{1}{R}\{mF([h, h+m],[m+1],-1) + hF([h, h+m] ,[m+1],-1) - \frac{2h(m+h)}{m+1} F([h+1, h+m+1], [m+2],-1)\} = C_m^+ R^{m+2h} 2^h F([h, h+m], [m+1],-1) \cdot \frac{J_m(kR)J_m'(kR) + Y_m(kR)Y_m'(kR)}{(J_m^2(kR) + Y_m^2(kR))} \quad (4.18)$$

Equation (4.18) is a transcendental equation and can be utilized for finding the eigenmodes of GRIN microresonator by graphical solution method. All parameters in equation (4.18), except m, are known. Here we predetermine m by the results of FDTD method (Taflove, Hagness 2005) to ease the comparison. Generally, for every m, we have valid solutions given by the analytical method.

4.4. Numerical Analysis of 2D MFE

We consider a 2D MFE microresonator closely coupled to a straight dielectric waveguide as shown in Figure 4.2. The MFE is excited by placing an electromagnetic source in the waveguide. We note that, the existence of the waveguide would shift the resonance frequency and may cause slight deformations in the resonant modes' field distribution. But, as we will demonstrate later in this chapter, there is a good agreement between the field distribution inside of MFE in two cases, with and without the optical waveguide. We consider optical waves propagating in the $x-y$ plane with electric field intensity vector polarized perpendicular to the plane (TE modes whose magnetic and electric field components are, H_x, H_y and E_z respectively).

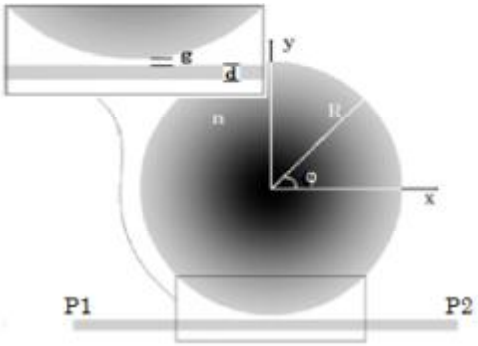

Figure 4.2. The chacteristic parameters of 2D Maxwell's fish eye. The locations of input (P1) and out put (P2) ports.

By imposing an appropriate excitation source for waveguide, the resonance spectrum of MFE can be found. A Gaussian source with broad band width is located in port P1 and the transmission of waveguide is monitored in port P2. The locations of ports are shown in Figure 4.2.

The transmission spectrum of the waveguide coupled to MFE can be obtained as Figure 4.3. The dips in this normalized spectrum show resonance modes of MFE in terms of normalized frequencies. By choosing one set of these resonance modes we can excite the system by continuous sources. The frequencies of new sources can be selected easily from Figure 4.3. Consequently, the coupling snapshots in the steady state can be extracted and these snapshots give us the related azimuthal mode number of MFE, specifically m number. Figure 4.4 shows the FDTD simulations for normalized frequencies of $a/\lambda = 0.2282,\ 0.2291, 0.2304$ and 0.2315 that result $m = 22, 23, 27$ and 29 respectively. $\lambda = \lambda_0/n$ and a is defined as $\Delta x = \Delta y = a/20$, where Δx and Δy are the grid sizes of the 2D Yee lattice in FDTD method (Arfken, Weber 2005). The refractive index of MFE is set according to equation (3.1) with $n_0 = 3.4641$. The radius of MFE is set to $R = 12a$, linear waveguide width is $d = a$ and the gap between waveguide and MFE is $g = 0.4a$. The perfect matched layer (PML) boundary condition has been used around the simulation domain and the last slide has been showed for time step

$7000\Delta t$ (Arfken, Weber 2005). Simulations were performed with the FDTD method, using MEEP, freely available software package (Oskooi et al, 2010).

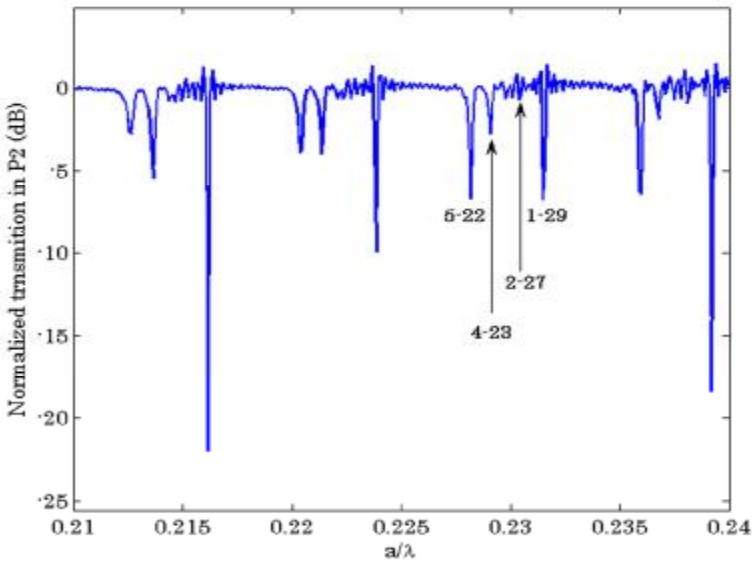

Figure 4.3. Normalized transmission spectum of waveguide in port P2 showing resonaces modes of MFE.

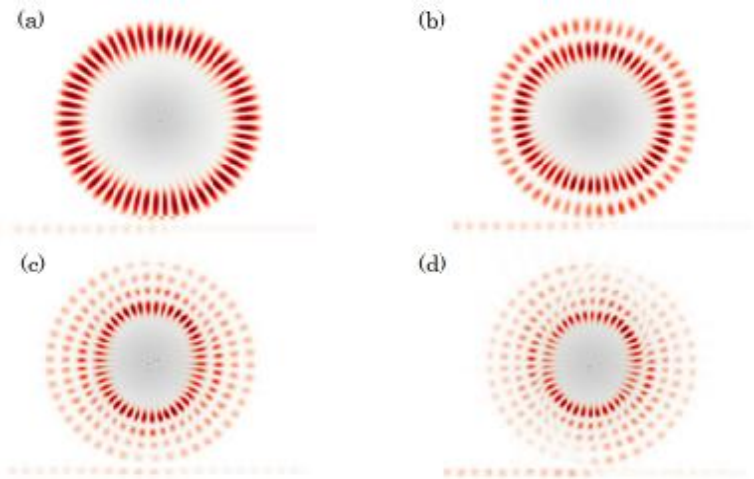

Figure 4.4. E-field intensity profiles for (a) $n=1,\ m=29$, (b) $n=2,\ m=27$, (c) $n=4,\ m=27$, (d) $n=5,\ m=22$

By inspecting the resonance frequencies of MFE in Figure 4,3, one can straightforwardly excite different modes sustained in the MFE microdisc. WGM behavior of the modes circulating around and inside the structure is apparent in Figure 4.4 and Figure 4.5. We should note that Figs. 4.4(a)-(d) are intensity plots. Figure 4.5 is amplitude profile.

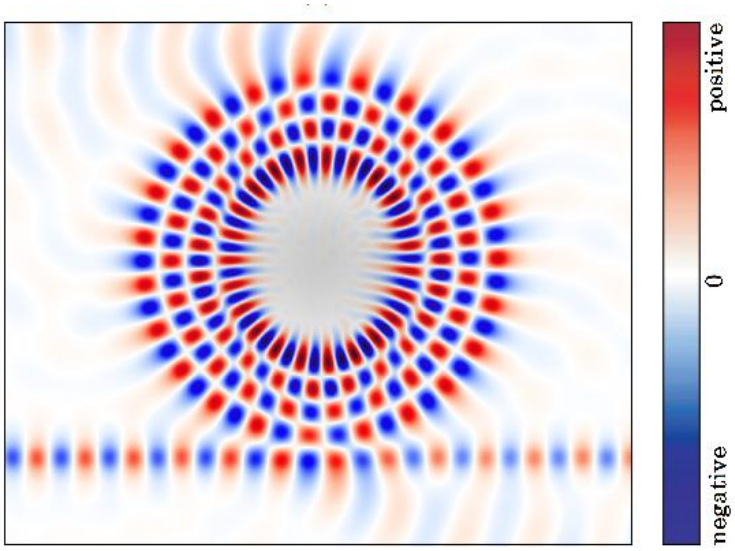

Figure 4.5. E-field distribution of MFE coupled optical waveguide for $n = 4, m = 23$.

4.5. Modes of 2D MFE

After determination of the azimuthal mode number m via FDTD simulation, we can turn to equation (4.18) and find the radial modes by graphical solving of this equation. The results give us only the orders of radial modes n. Since WGMs are confined inside of microresonator, to find the positions of radial modes or radial maximums and minimums of electric field, we use $\P E_z^{in} / \P r = 0$ relation for $r \mathbf{p} R$ or $x \mathbf{p} 1$. Accordingly, the following expression is obtained:

$$m\mathrm{x}^{m-1}(1+\mathrm{x}^2)^{\mathrm{h}}F([\mathrm{h},\mathrm{h}+m],[m+1],-\mathrm{x}^2)+2\mathrm{x}^{m+1}(1+\mathrm{x}^2)^{\mathrm{h}-1}$$
$$F([\mathrm{h},\mathrm{h}+m],[m+1],-\mathrm{x}^2) \qquad (4.19)$$
$$=\frac{2\mathrm{h}(\mathrm{h}+m)}{m+1}\mathrm{x}^{m+1}F([\mathrm{h}+1,\mathrm{h}+m+1],[m+2],-\mathrm{x}^2).$$

By graphically solving of equation (4.19), for a given azimuthal mode m, the exact locations of the radial modes n can be extracted. Now, all characteristics of WGMs are known. Figure 4.6 shows the result for $m=23$ and $n=4$. The four intersect points in this figure are $\mathrm{x}=0.494$, 0.632, 0.755 and 0.884 which determine the radial peaks and valleys of the electric field corresponding to specific mode.

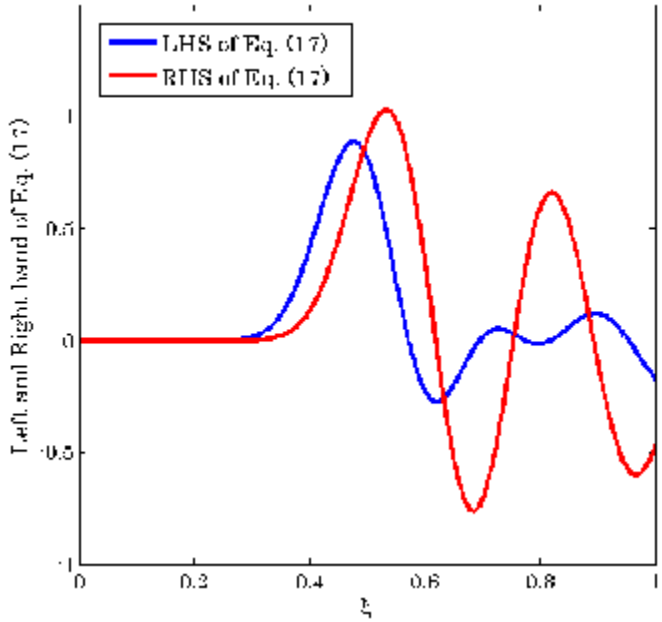

Figure 4.6. Graphical solution of equation (4.19)

Additionally, the radial component of electric field inside the MFE can be written from equation (4.13) as:

$$\Psi_m^{in}(x) = \sum_m \{x^m (1+x^2)^{\eta} F([\eta, \eta+m], [m+1], -x^2)\}. \quad (4.20)$$

Figure 4.7 shows $\Psi_m^{in}(x)$ expressed in equation (4.20) for the inside region of MFE. We can make a comparison between Figures 4.6 and 4.7 such that the locations of peaks and dips in Figure 4.7 exactly correspond to intersection points between the two curves plotted in Figure 4.6 .

Figure 4.8 shows the electric field distribution inside of MFE as defined by Eq. 4.17(a) for $n = 4$ and $m = 23$. When we compare the analytical result shown in Figure 4.8 with the numerical one presented in Figure 4.5 we see that there is a good agreement between the two approaches. In plotting Figure 4.8 the straight waveguide is not considered. The close agreement between the two methods supports the idea that the presence of optical waveguide does not strongly perturb the MFE microdisc.

The properties of disc and ring microresonators have been studied from both theoretical and experimental standpoints (Vahala 2003, Quan, GUO 2009, Prkna et al 2004). In the proposed configuration the microdisc of usual waveguide-resonator configuration has been replaced by a MFE lens. To the best of our knowledge, the idea of replacing the microdisc with a GRIN medium has been proposed in this thesis for the first time. Although the design and fabrication of GRIN devices by using traditional approaches such as continuously varying doping on natural dielectric media are not very practical, but the emerging disciplines of artificial dielectrics will open up possibilities to realize spatially varying or GRIN devices such as MFE lenses (liu et al, 2013).

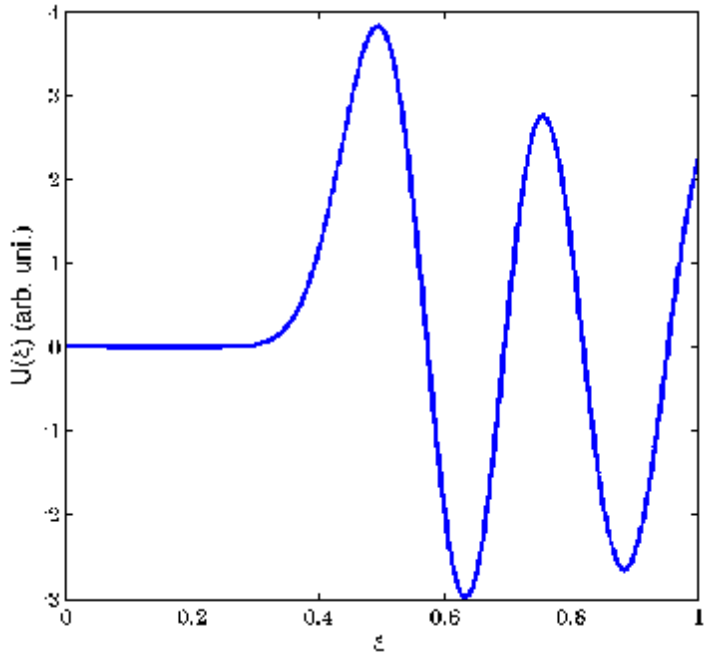

Figure 4.7. Radial component of electric field inside region of MFE.

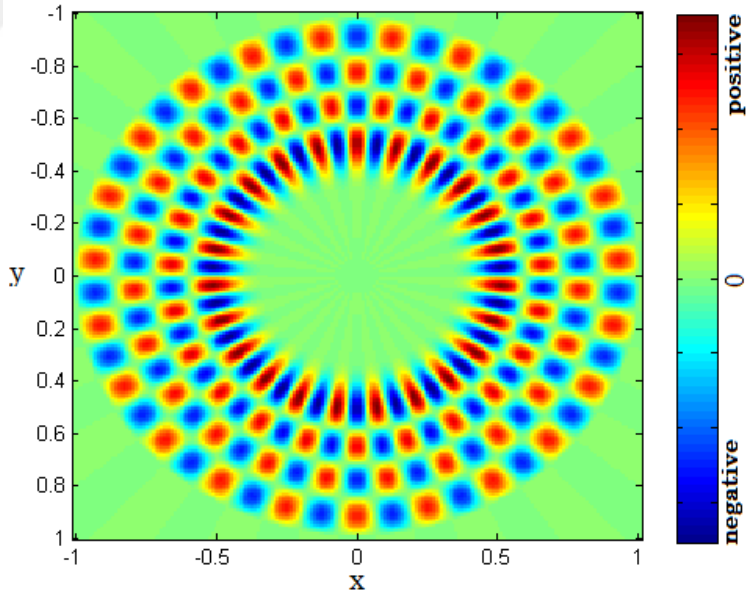

Figure 4.8. Electric field distribution inside of 2D MFE for $n = 4$ and $m = 23$.

The significance of the present study lies not only being a new type of microresonator but also possessing a rich resonance characteristics. In conventional microresonator the coupled modes penetrate only the region near the edges, but in MFE, the coupled modes can penetrate more towards the core region as showed in Figures (4.4) and (4.5).

In the numerical studies when the refractive indices of the waveguide and disc resonator are taken to be 1.7321, the quality factor becomes 188 at the normalized frequency $a/\lambda = 0.2266$. On the other hand, MFE resonator with a variable refractive index (increasing from 1.7321 at the edge to 4.4641 at the center) sustains quality factor of 1146 at the normalized frequency $a/\lambda = 0.2291$. We should note that increasing the refractive index of the disc resonator enhances the field confinement; hence, quality factor is expected to increase.

4.6. Spectral Properties of 2D MFE

In general, the WGMs in dielectric optical resonator are function of the morphology, that means geometry and refractive index of the resonator and the surrounding medium play important role (Schweiger et al 2006). The morphology dependence of these structures encouraged us to examine more complex spherical/cylindrical dielectric aiming to obtain higher quality factor, and rich optical properties (Chremmos et al 2010). We studied the spectral properties, Q factor and free spectral range (FSR) of WGMs in a 2D MFE and compared the results with 2D conventional microdisc ones.

The conventional disc has constant refractive index $n_0/2$, radius R and the MFE has refractive index n_0 in the center decreasing to $n_0/2$ at the rim according to equation (4.1) and its radius is R as have been shown in Figure 4.2. They are closely coupled to a straight dielectric waveguide. A Gaussian source with broad band width is located in ports P1 to excite the systems and the

transmissions of waveguides are monitored in ports P2. All other characteristic parameters are the same as the previous section. The parameter n_0 in the refractive indices of the disc and MFE is set to 3.4641. The radius for both microresonators is set to $R = 12a$. a is defined as $\Delta x = \Delta y = a/20$. The linear waveguides refractive index is $n_0 / 2$ and their widths are $d = a$. There is not any gap between waveguides and microresonators. The perfect matched layer (PML) boundary condition has been used around the simulation domain. The normalized transmission spectrums of the waveguides coupled to disc and MFE are shown in Figure 4.9. The time steps for all simulations are $7000\Delta t$.

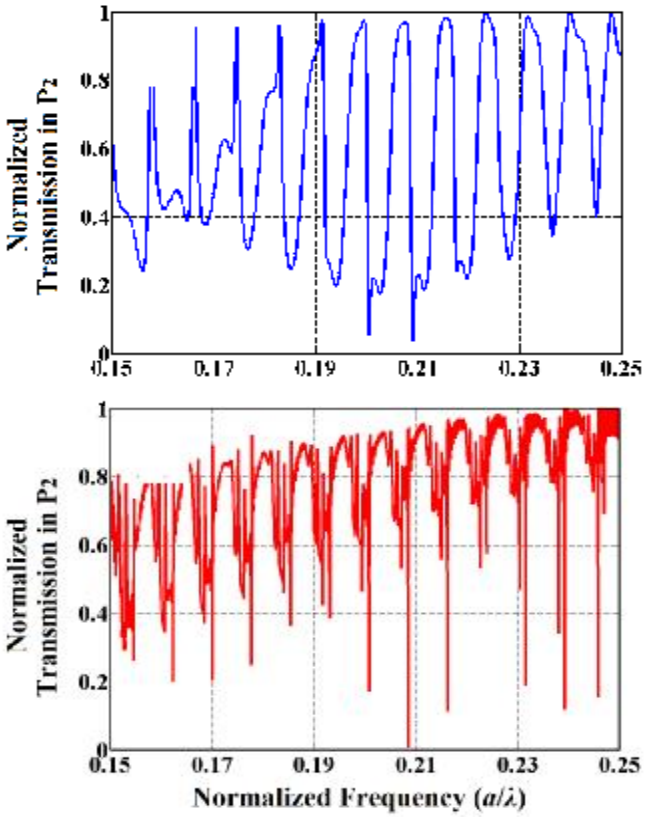

Figure 4.9. Normalized transmission spectra of the (a) conventional microdisc and (b) 2D MFE

We see from these figures that MFE refractive index, equation (4.1), has two effects: The resonances of disc have been shifted, when it has been changed to graded index medium one. These shifts are clearly shown in Table 1, as well. On the other hand, the MFE microresonator displays mode splitting in the vicinity of its resonances.

Table 4.1. Calculated quality factor and free spectral range for conventional 2D microdisc and 2D MFE

Conv. Disc			MFE		
Freq.	Q	FSR	Freq.	Q	FSR
0.1601	22	0.0081	0.1545	811	0.0077
0.1682	23	0.0083	0.1622	850	0.0077
0.1765	40	0.0085	0.1699	888	0.0077
0.1850	43	0.0088	0.1776	926	0.0077
0.1938	44	0.0088	0.1853	965	0.0076
0.2026	44	0.0086	0.1929	965	0.0078
0.2112	45	0.0084	0.2007	2084	0.0077
0.2196	51	0.0083	0.2084	2161	0.0077
0.2279	54	0.0085	0.2161	2238	0.0076
0.2364	64	0.0085	0.2238	2314	0.0076
0.2449	111		0.2314	2391	0.0142
			0.2456	2456	

Figure 4.10 represents the Q factor for all resonances of conventional disc and major resonances of MFE. Clearly, there is notable increase in magnitude of Q in MFE. Table1 contain Q factors for these two cases. The free space between consecutive resonances is known as free spectral range (FSR) (Chremmos et al 2010). The information in Table 1 shows that the FSRs for two structures are very close to each other.

4.7. Fabrication Aspects

To fabricate the GRIN structure, one can follow the procedures provided in Falco et al (2011) and Gabrielli et al (2011). The effective refractive index of any transparent material such as polymer (low refractive index) or Silicon (high refractive index) depends on the thickness variation of the slab that guides the light. Thickness variation at the micron and nano scale can be achieved by means of advanced manufacturing techniques such as focused ion beam (Gabrielli et al 2011).

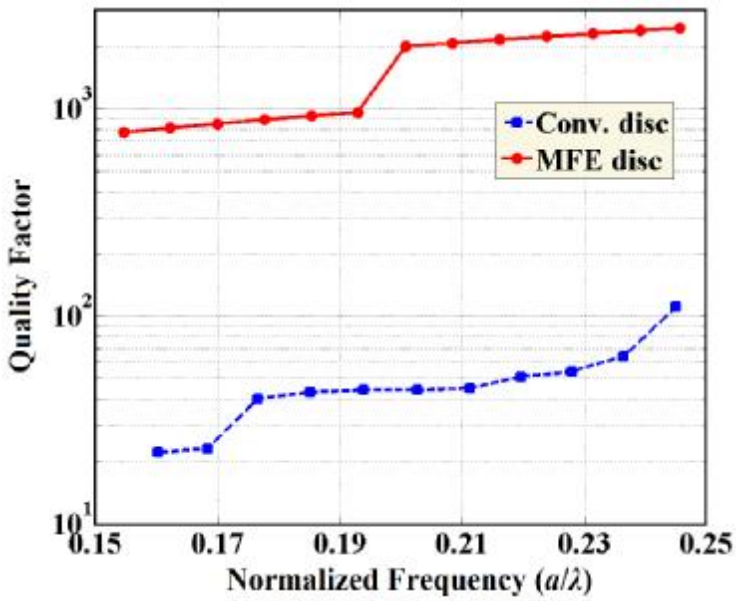

Figure 4.10. Quality factor, Q, for conventional microdisc and 2D MFE.

4.8. Conclusion

In summary, solutions of Helmholtz equation in spherical coordinates come in the form of eigenvalue problems. We have shown that the radial (n) and azimuthal (m) mode numbers can be obtained as eigenvalues of Helmholtz equation for 2D Maxwell's fish eye (MFE) microresonator. We have proposed 2D MFE for designing unconventional microresonator. In this new structure, we have

introduced an additional parameter, i.e. spatially varying refractive index to manipulate the spectra of optical modes in microdisc resonator keeping intact the size and shape. The 2D MFE resonator is laterally coupled to an optical waveguide and for numerical calculations we use finite-difference time-domain method. Analytical and numerical treatments of the design unveil the optical resonances of the structure.

While radially inhomogenous refractive index media based on metamaterials and plasmonics have been investigated for various applications ranging from optical cloaking to optical black holes, all-dielectric counterpart in integrated photonics is limitedly explored. The proposed 2D MFE resonator may pave the way for diverse integrated photonic applications rather than solely exploring the same structure for mostly imaging studies.

5. GRADED INDEX PHOTONIC MOLECULES

5.1. Introduction

Recent advances in material science and nano-fabrication techniques make possible the realization of novel microcavity-based optical components. This chapter introduces the fundamental optical properties of graded index (GRIN) photonic molecules (PMs). New functionalities of graded index PMs pave the way for their use as testbeds for the exploration of physical regimes in atomic physics and quantum optics.

When a circular microcavity is illuminated laterally with a laser beam, the resulted WGMs resemble to the confined electron states in atoms. In fact, one can transform the Maxwell equations into a Schrodinger equation that reveals modal functions that are analogous to wave functions of electrons in an atom. The WGMs are associated with photon confinement by a particle's dielectric potential. However, unlike states in a conventional atom, the modes of a photonic atom are virtual with the photon lifetime limited by leakage out of the particle (Arnold et al 1992). The leakage can be extremely slow.

In the photonic cases, at low refractive index dielectric microspheres or microdiscs, the WGMs contributing to photonic binding are always localized at the cavity surface, so they would be equivalent to atoms excited into high-energy orbitals (Shi et al 2012). Due to these similarities optical microcavities can be termed as photonic atoms (PA) (Wang et al 2011, Shi et al 2012). The most typical examples of PAs range from metallic nanoparticles (Gopinath 2009), to low refractive index dielectric microspheres or microdiscs (Ishii and Babaa 2005). In the former case, the high optical dissipation of metals is a big obstacle for developing devices. On the other hand, clusters of circular cavities with coupled WGMs have interesting spectral and optical transport properties (Li et al, 2014). Several mutually coupled photonics atoms form a photonic molecule (PM). The electromagnetic modes of the whole structure are very similar to the bonding

(symmetric) or antibonding (antisymmetric) electronic wave function modes formed in molecules (Wang et al 2011). Typical PM structures consist of two or more light-confining resonant cavities such as Fabry–Pérot resonators, microspheres, microrings, point-defect cavities in photonic crystal (PC) (Boriskina 2010). It is interesting to study the photonic molecule of various structures using optical techniques and it may further improve our understanding of the real molecular structures (Wang et al 2011). In principle, two or more microspheres close to each other allows optical coupling of the modes between the spheres, which results in a complex rearrangement of the mode structure in the strong coupling regime similar to the electronic molecular orbital in a chemical molecule (Bayer et al 1998). Specifically, photonic molecules are often modeled as two dimensional coupled dielectric disks. Based on the spatial configurations and the number of coupled microdisks, peculiar spectral features such as mode-splitting and enhancement in Q-factors could be achieved (Boriskina 2006).

Unique optical properties of PAs, including light confinement in compact structures, high quality factors, and sensitivity to environmental changes have made them attractive building blocks for a variety of applications in basic science, information processing, and biochemical sensing (Boriskina 2010).

Optical properties of complex PMs depend on mutual coupling between all the cavities forming the PM and can be optimally tuned by adjusting the sizes and shapes of individual cavities as well as their positions

5.2. MFE Microcavity as a Photonic Atom

In this section we study a simplified 2D MFE microdisc for understanding the underlying physical properties of 3D MFE as photonic atom. The MFE microdisc is assumed to have a refractive index profile relative to radial distance, r, as shown in Equation (4.1). A conventional microdisc having the refractive index of $n_0 / 2$ and a MFE with refractive index of $n(r)$ are assumed to side-exciting by

using a dielectric waveguide with the refractive index of $n_w = n_0 / 2$, separately. The schematic representations of both structures are illustrated in Figures 5.1(a) and (b) and side-exciting do as shown in 5.1(a). In our case, the n_0 and R are set to be 3.4641 and $2.79\,\mu m$.

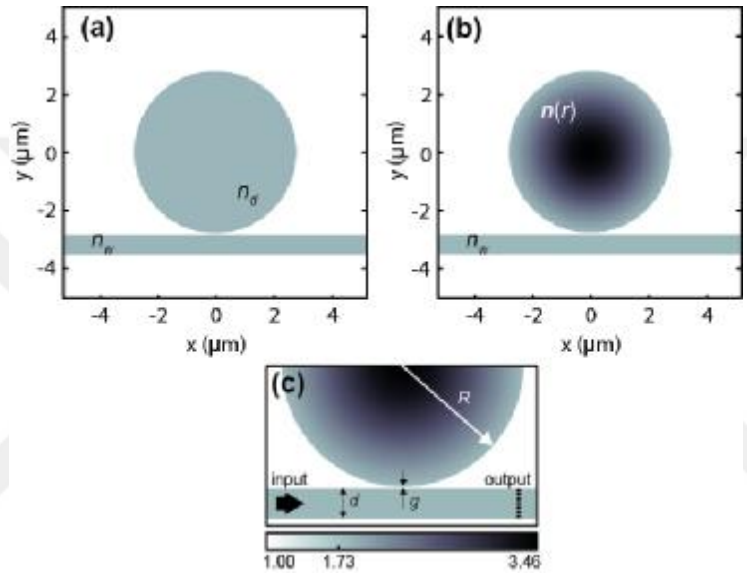

Figure 5.1. The schematic of the: (a) conventional microcavity and (b) (MFE) coupling to the bus waveguide. (c) Input and output ports, physical characteristics of microcavities.

For a given PA or PM the spectral characteristics which are represented by the total number of the split components and their spectral shifts are named spectral signatures (Li 2017). The spectral signatures mainly are representative of number of constitutive atoms, topology and symmetry of structure. In Figures 5.2(a) and (b) we have showed the spectral signatures of normal disc and MFE respectively. The numerical simulations were performed by FDTD method with commercial software by Lumerical (Lumerical 2017) and were tested by MEEP program (Oskooi et al 2010). In Lumerical calculations, a Gaussian modulated pulse of 6 femtoseconds (fs) width was launched into the input port of waveguide

as illustrated in Figure 5.1(c). The electric vector of input electromagnetic waves was polarized in direction normal to the plane (TE mode was investigated). For all calculations, the shut-off criteria of 10^{-5} have been used. In this condition, the electric field in the computational domain is less than 10^{-5} of the input field and the convergence of results is guaranteed.

One of the important observations is that the transmission spectrum of MFEs is considerably more sophisticated compared to their conventional counterparts. Instead of each mode in conventional disc there is a supermode, containing three modes, in MFE. The narrow WGM peaks in supermodes allow observations of fine splitting effects related to refractive index varying of PA. To be clearer, we calculated the Q factor in both systems. The Q-factor in the conventional microdisc is $Q = 172$ at the resonance wavelength of 1551 nm, whereas in MFE this value reaches up to $Q_1 = 751$, $Q_2 = 505$, $Q_3 = 382$ for resnonce modes of 1503 nm, 1515 nm and 1530 nm respectively. The resonance modes in conventional microdisc have free spectral ranges (FSR) of 91 nm in the vicinity of 1550 nm. For MFE the FSR of supermodes is 88. That large difference in Q-factors implies that the MFE microcavities are more useful for high quality sensing systems.

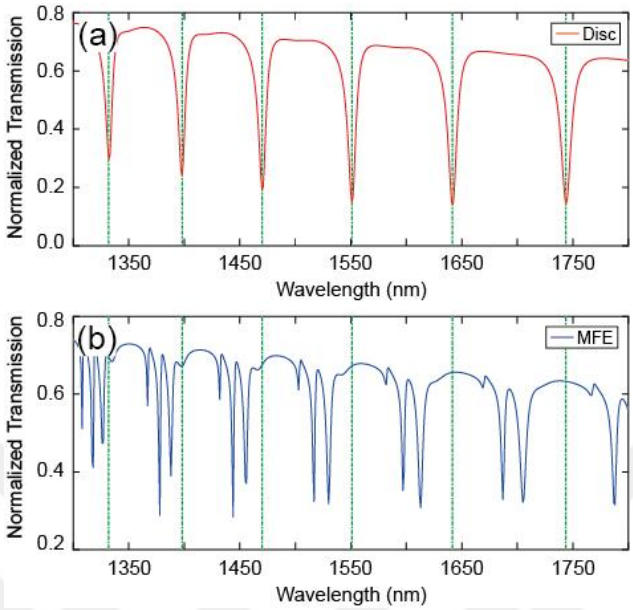

Figure 5.2. The normalized transmitted E-field (spectral signatures) for (a) conventional microdisc and (b) MFE. There are shifting to the left and broadening of supermodes in MFE

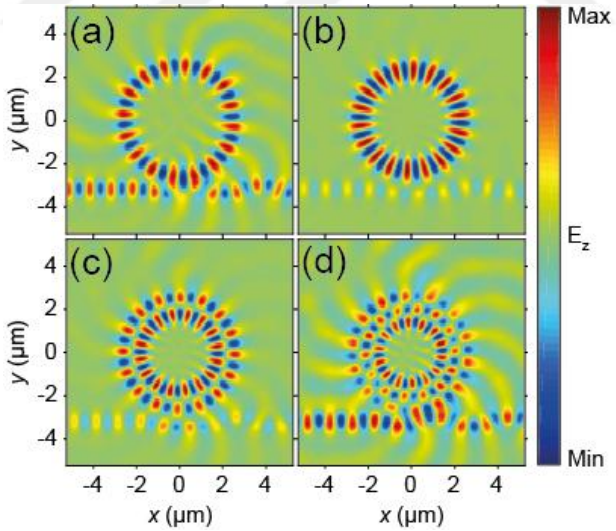

Figure 5.3. Spatial E-field distribution for (a) conventional microdisc at $\lambda = 1551nm$. Spatial E-field distribution for MFE: (b)$\lambda_1 = 1503nm$, (c)$\lambda_2 = 1515nm$ and (d)$\lambda_3 = 1530nm$.

After obtaining the transmission spectrum (spectral signatures) of both structures the spatial electric field (E-field) distribution was obtained by launching continuous wave source into the input port of waveguide at each desired mode. The spatial distribution of electric field for uncoupled modes in convensıonal microdisc and for one supermode for MFE are shown in Figure 5.3.

5.3. Spatial Configurations of MFE for Photonic Molecule

The sharp resonances of supermodes in single MFE encouraged us to study the spectral features of clusters of MFEs. Using microspheres as classical PAs, we can assemble them in a wide range of structures including linear chains and planar geometries. These configurations can be investigated as PMs.

In this section, we are studying four different configurations of PMs including three linear chains with two, three and four PAs and a quadrumer formed by 4 circular resonators as planer structure. All the structures are schematically shown in insets of Figures 5.4 and 5.6. In order to find the spectral signature of each configuration, the FDTD simulations were performed for different combinations of the structural parameters. For all structures, corresponding normalized transmissions (spectral signatures) are obtained as done in the last section for simple structures. The simulation tool is Lumerical software too. Figures 5.4(a),(b) and 5.6(a),(b) show the normalized transmissions (spectral signatures) of the studied structures. The green dashed lines in each figure shows the uncoupled mode of conventional disc for comparison and showing the left shifting of supermodes.

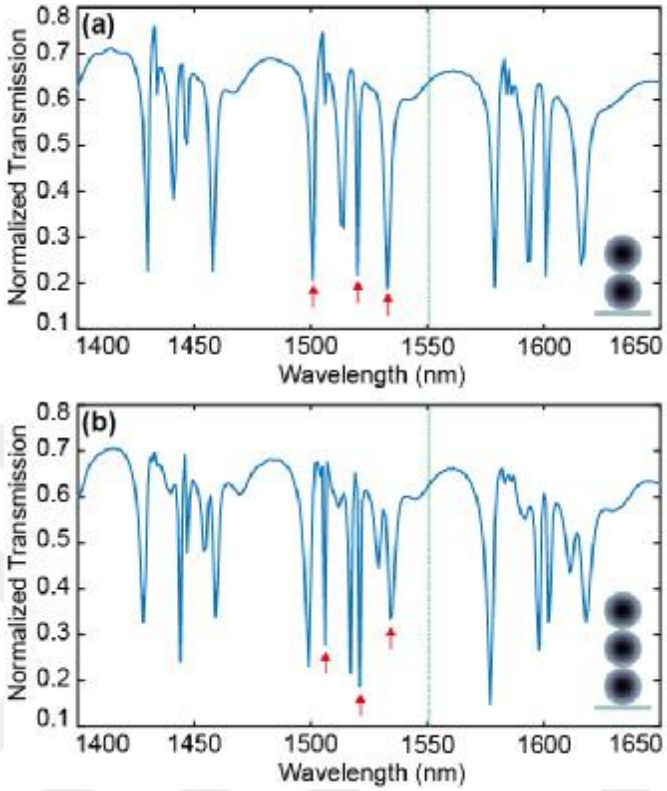

Figure 5.4. The transmission spectrum of PMs. (a) Linear chain with two MFE. (b) Linear chain with three MFE. The arrows show the wavelength selected to simulate the electric field distributions.

As mentioned in the previous section we can obtain the Q-factor for each mode from transmission spectrum. We have selected three modes from the supermode nearing of the uncoupled mode of conventional microdisc (1551nm). Three red arrows show the wavelength of selected mode in each figure. The results are summarized in Table 5.1. The results of previous section for conventional microdisc and single MFE are added in two first rows for comparison.

It is deduced from results showed in Table 5.1 that the quality factor of resonances in supermodes are much greater than in the parent conventional microdisc, about nine times in quadrumer ($l_2 = 1524\,nm$). It seems we can introdue structures with the optical supermodes (Boriskina 2007, Boriskina 2010)

by employing these GRIN PMs. Also, it can be resulted from the transmission spectra in Figures 5.4 and 5.6 that the large number of resonances in each supermodes appear when the number of coupled PAs are increased, which indicates the possibility to have wavelength selectivity in the PM structures. In addition, there is the potential of wavelength switching with the PM structures. Lastly, it should be noted that in the previous section we had mode splitting in uncoupled MFE or GRIN PA. Now, in coupled MFEs or PMs the effect of mode hybridization (Li et al 2017) occurs.

Table 5.1 Calculated Q-factor for 2D Microdisc, Uncoupled MFE as Photonic Atom (PA) and various Photonic Molecules (PMs). The selected wavelengths (WLs) are shown in related figure with red arrows.

	λ (nm)	Q	Radial mode (***n***)	Angular mode (***l***)
Disc	1551	182	1	16
1 atom (MFE)	1502	757	1	18
	1515	505	2	16
	1530	382	3	14
2 atoms chain (Selected WLs)	1501	750	1	19
	1520	760	2	17
	1533	511	3	15
3 atoms chain (Selected WLs)	1506	1506	1	19
	1521	1521	2	17
	1534	307	3	15
4 atoms chain (Selected WLs)	1505	1505	1	19
	1519	759	2	17
	1531	765	3	15
Quadrumer (Selected WLs)	1499	1249	1	19
	1524	1016	2	17
	1537	768	3	15

Based on information of transmission spectrum, we can reach to field map or field distribution of each mode. We have selected three modes form supermode near 1551 *nm* for each MP. The selected modes are addressed by red arrows in Figures 5.4 and 5.6. The Figures 5.5 and 5.7 show the E-field distributions of selected modes. The energy transfer along the elements of PMs can be achieved through nearest neighbor interactions between adjacent cavities (photon hopping) (Boriskina 2010).

We can see a noticeable point in Figure 5.7(c) which the E-field is concentrated in two side resonators, while the two central ones are almost dark. This effect has been seen in the other PMs too. In the 3 atoms chain, the mode with $\lambda = 1879\,nm$ and in the five atoms chain the mode with $\lambda = 1909\,nm$ the central atom is completely dark as can be seen in Figure 5.8. For linear chains this can be explained by the Bloch modes formation in the coupled molecule (Li et al 2017, Möller et al 2007). According to Möller et al explanations, among the eight split modes in a four atoms chain, light blue colored region in Figure 5.6(a), the mode $\lambda_3 = 1531\,nm$ dominant for the first and the Fourth microresonator.

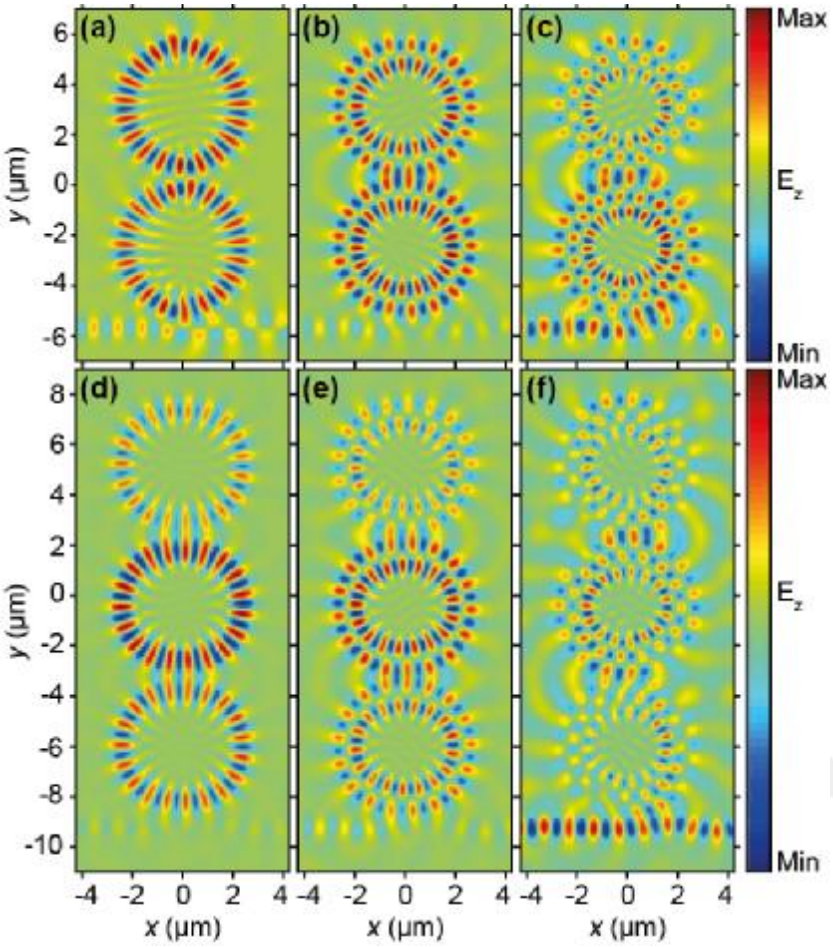

Figure 5.5. Spatial E-field distribution for two atoms chain: (a) $l_1 = 1501nm$, (b) $l_2 = 1520nm$ and (c) $l_3 = 1533nm$. Spatial E-field distribution for three atoms chain; (d) $l_1 = 1506nm$, (e) $l_2 = 1521nm$ and (f) $l_3 = 1534nm$.

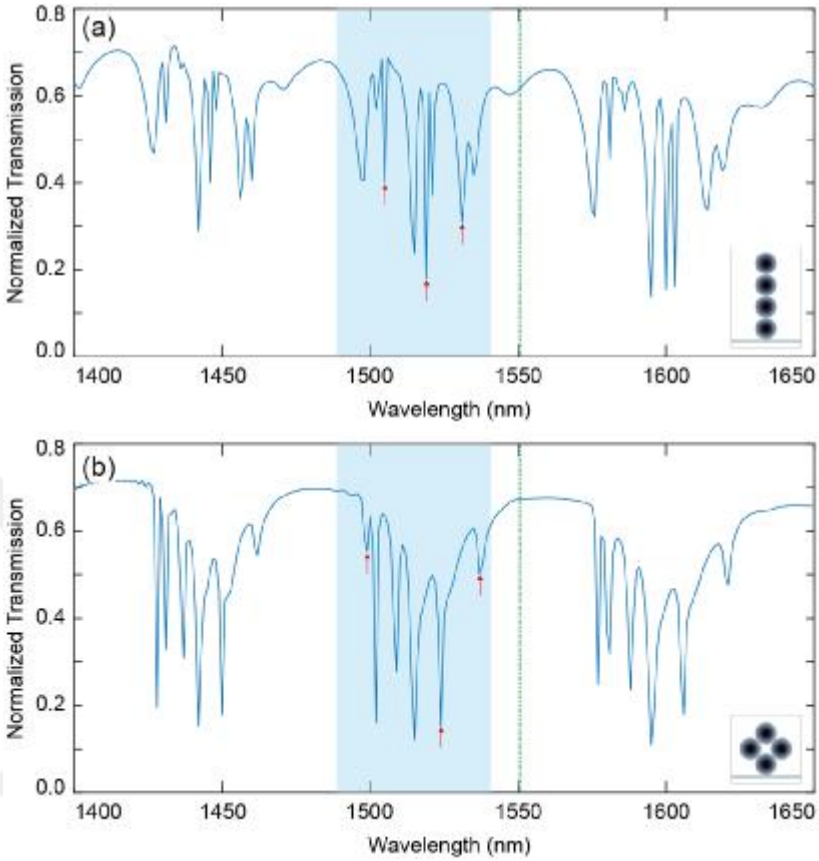

Figure 5.6. The transmission spectrum of PMs. (a) Linear chain with four MFE. (b) Quadrumer. The arrows show the wavelength selected to simulate the electric field distributions.

The radial (n) and angular (l) mode numbers of specific resonances are also explored to better understand the WGM features in coupled MFE microresonators as PMs. For this purpose, various resonant wavelengths are selected from the transmission spectra of PMs from Figures 5.4 and 5.6, in which some regarding wavelengths are marked by red arrows in the figures. The calculated field (E-field) distributions are demonstrated in Figures 5.5 and 6.7. As done in the previous section, the electric vector of input electromagnetic waves was polarized in direction normal to the plane (TE mode was investigated). Here, some of concerned E-field may become more complex in comparison to single atom case.

The corresponding radial and angular mode numbers for different structures are listed in the Table 5.1.

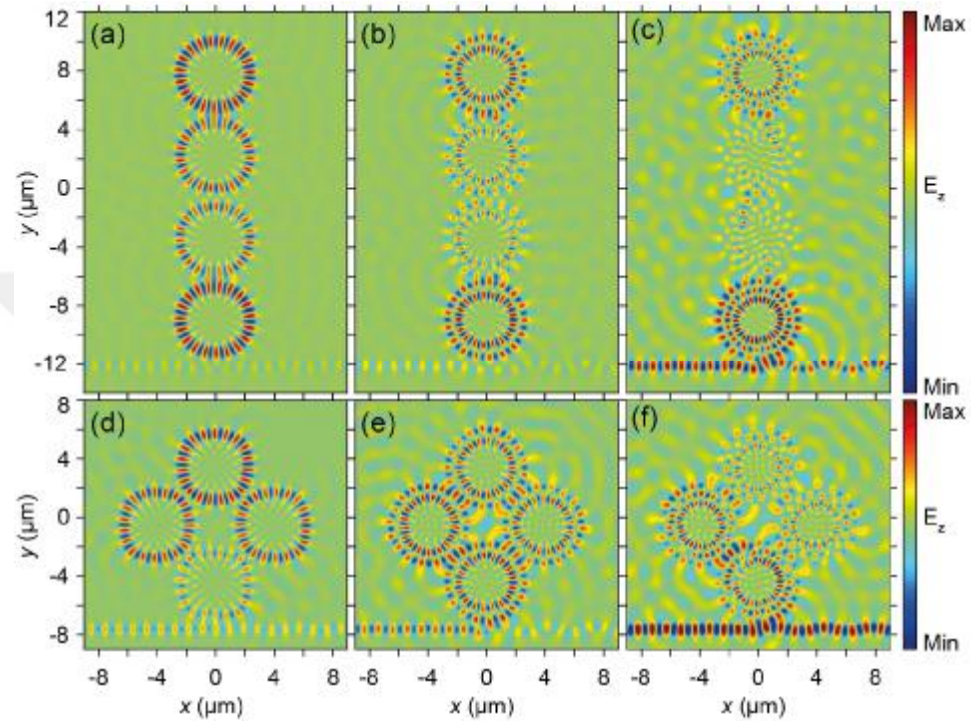

Figure 5.7. Spatial E-field distribution for 4 atoms chain: (a) $l_1 = 1505\,nm$, (b) $l_2 = 1519\,nm$ and (c) $l_3 = 1531\,nm$, Spatial E-field distribution for Quadrumer: (d) $l_1 = 1499\,nm$, (e) $l_2 = 1524\,nm$ and (f) $l_3 = 1537\,nm$.

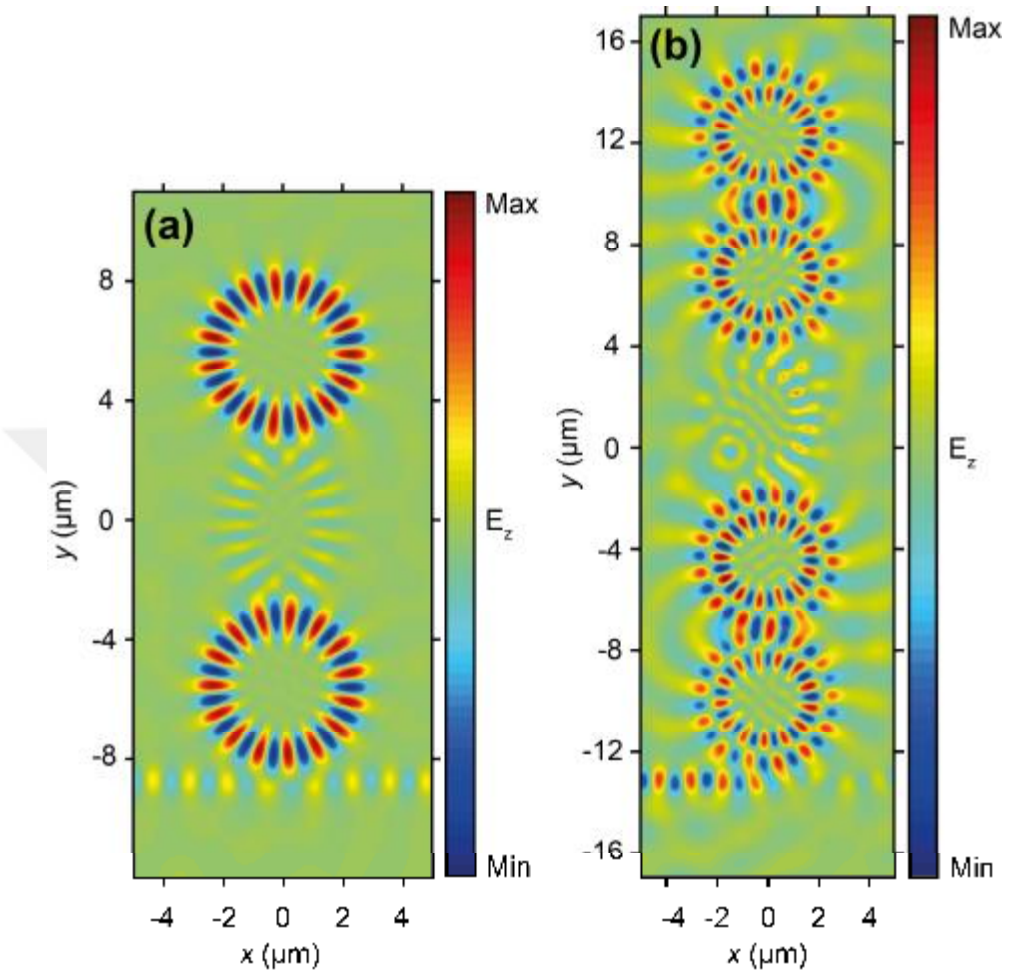

Figure 5.8. Spatial E-field distribution for (a) 3 atoms chain at $\lambda = 1879\,nm$, (b) 5 atoms chain at $\lambda = 1909\,nm$.

5.4. Conclusion

In this chapter, the coupling behaviors of optical modes in PMs formed by two or more MFEs have been investigated. Each PM has certain spectral property which is related to the topology and geometry of a given molecular configuration and contrast between refractive index of PM and surrounding medium. The varying of refractive index of PM has been mentioned in our work.

In a single MFE as PAs the mode splitting is occurred. This PA has sharper resonances than the conventional microspheres.

In PMs the couplings between WGMs with different radial and angular mode numbers are observed, resembling the mode hybridization of atomic orbital in chemical molecules. So, it seems that in GRIN PMs we observe the mode hybridization. The supper-modes are formed in small structure (finger prints) in comparison to other works. The number of atoms and refractive index variation determine the number of spectral components which can be split or remain degenerate depending on the symmetry. The unique characteristics of GRIN PMs make possible the realization of ultra-compact on-chip optical delay lines and biosensors.

6. PARITY-TIME- (PT-) SYMMETRY IN MICRORING RESONATORS[1]

6.1. Introduction

In the Dirac–von Neumann formulation of quantum mechanics, the Hamiltonian, H , of all physical systems is represented by Hermitical operator on a Hilbert space (Shankar 1994). The Hermiticity of H is expressed by the equation

$$H = H^{\dagger}. \tag{6.1}$$

The symbol † represents the operations of matrix transposition combined with complex conjugation. The mathematical symmetry condition (6.1) implies that the eigenvalues of H are real and the time-evolution operator $T = e^{-iHt}$ is unitary (Bender 2007). In other words, the energy eigenvalues are real and the wave function norm remains invariant with time (Shankar 1994).

In 1998, Bender and Boettcher showed that it is possible to describe natural processes by means of non-Hermitian Hamiltonians (Bender 2007). They showed that the mathematical Hermiticity requirement (6.1) can be replaced by the analogous but physically transparent condition of space–time reflection symmetry or Parity-Time- (PT-) symmetry:

$$H = H^{\mathrm{PT}} \tag{6.2}$$

without violating any of the physical axioms of quantum mechanics (Bender 2007). In equation (6.2) P represents the space-reflection operator, or parity operator. P is a linear operator. T represents the time-reversal operator and it is not a linear

[1] This chapter is based on: Giden, I. H., Dadashi, Kh., Botey, M., Herrero, R., Staliunas, K., Kurt, H., 2015. Nonreciprocal light transmission in gain-loss modulated micro ring resonators. In Transparent Optical Networks (ICTON), 17th International Conference. IEEE.

operator. PT-symmetric Hamiltonian need not be Hermitian. Thus, it is possible to have a fully consistent quantum theory whose dynamics is described by a non-Hermitian Hamiltonian (Bender 2007). By pioneering work of Bender and his colleagues new kinds of Hamiltonians were introduced in which the mathematical condition of Dirac Hermiticity (6.1) has been replaced by the physical condition of PT-symmetry (6.2). In the general form of the time-independent Schrodinger eigenvalue problem we have the equation:

$$H\psi = E\psi \ , \tag{6.3}$$

in which ψ and E are the eigenstate (or eigenfunction) and eigenvalue of H respectively. Let us assume that ψ be is an eigenstate of the PT operator too.

$$PT\psi = l\psi \tag{6.4}$$

The general formalism of PT-symmetric quantum mechanics implies that, if every eigenstates of a PT–symmetric Hamiltonian is also an eigenstates of the PT operator, the PT-symmetry of H is unbroken. In this case, the potential associated with Hamiltonian obeys:

$$V(\mathbf{r}) = V^{*}(-\mathbf{r}) . \tag{6.5}$$

It shows a necessary condition (but not sufficient) for a Hamiltonian to have unbroken PT-symmetry. It is required that the potential energy operator is even in its real part while odd in its imaginary (Guo et al 2009).

Conversely, if some of the eigenstates of a PT-symmetric Hamiltonian are not simultaneously eigenstates of the PT operator, the PT- symmetry of H is broken (Bender 2007).

The formal similarity between the Schrodinger equation and the wave equation in optics made it possible to realize complex PT-symmetric potentials within the framework of optics (Guo et al 2009).

In optics, the PT-symmetry condition on the potential associated with Hamiltonian, translated to the complex refractive index,

$$n(\mathbf{r}) = n^{*}(-\mathbf{r}). \tag{6.6}$$

$$n(\mathbf{r}) = n^{real}(\mathbf{r}) + in^{img}(\mathbf{r}), \tag{6.7}$$

which implies that the real part of the refractive index, $n^{real}(\mathrm{r})$, is symmetric, while the imaginary part, $n^{img}(\mathrm{r})$, is asymmetric. Various theoretical and experimental studies carried out in optical PT-symmetric systems. New features such as PT phase transitions, asymmetric light propagation, unidirectional invisibility, asymmetric chirality. The pioneering works investigated in 1D and 2D PT-symmetric systems were also considered (Turduev et la 2015, Regensburger et al 2012) as the basis of the development of novel devices. Nevertheless, to date a limited number of the reported studies investigate PT-symmetry in ring geometries (Giden et al 2016, Peng et al 2014, Feng et al 2014).

On the other hand, ring resonators have a special place in integrated photonic devices. Due to their small size, however much larger than the optical wavelength, such resonators are expected to support a large number of closely spaced multiple resonances. Therefore, these structures when side-coupled to signal waveguides behave as spectral filters, thereby allowing compact wavelength division multiplexing applications (WDM) (Little et al 1997).

In this chapter, a new type of add-drop microring resonator is proposed that is made up of gain and loss materials. In all-dielectric linear systems, light transmission is reciprocal: A symmetric transmission spectrum is observed when

an incident source is pumped from one side and output power detected in the other side or vice versa. On the other hand, PT-symmetric optical systems that consist of balanced gain-loss modulation possess unique characteristics such as unidirectional beam propagation, asymmetric light transmission and nonreciprocal chirality. It is numerically proved that PT-symmetric optical resonator designs can be achieved by properly arranging the gain-loss modulation so that different resonant modes can be promoted depending on the direction of source incidence. Corresponding transmission of the ring resonant modes operates in the telecommunication wavelength range $1.5 - 1.7\,\mu m$.

6.2. The Structure

Ring resonators have a special place in integrated photonic devices due to small sizes and supporting multiple resonances. These types of photonic structures behave as a spectral filter thereby allowing WDM applications. In this chapter, an add-drop microring resonator is designed that include balanced gain-loss materials and proposed for the enhancement of nonreciprocal resonant modes. The designed structure with its geometrical parameters is schematically represented in Figure 6.1(a). It consists of two Si-waveguides having a width of $w = 0.31\,\mu m$. These waveguides are coupled to a ring resonator whose radius and thickness sizes are set to $(R, r) = (2.79\,\mu m, 0.62\,\mu m)$. The up and down waveguides are made of Si with a refractive index of $n_{wg} = 3.46$ at the telecom wavelengths. The ring resonator contains two adjacent regions as can be viewed from Figure 6.1(a): Blue half (left semicircle) of the ring is composed of a synthetic gain (G) material having a complex index of $n_G = n_{Si} - j0.01$ while the red half (right semicircle) is formed by a lossy (L) material whose refractive index is fixed as $n_L = n_{Si} + j0.01$. The spacing between up/down waveguide and the ring resonator is kept as $s = 0.20\,\mu m$.

Our design includes four ports. When an incident beam is launched from Port 1 (red rows), it couples to the ring resonator and at resonant frequencies, the coupled light rotating the ring encounters a circularly 1D PT symmetric structure as in Figure 6.1(b), viz. loss-gain modulated structure in one dimension. On the other hand, in the case of source incidence via Port 4, the light at resonance circulates the ring and meets a 1D gain-loss modulated PT system, as shown in Figure 6.1(c). In that case, resonant modes occurring in forward and backward incidences may undergoes nonreciprocal coupling due to symmetry breaking effect of 1D PT symmetric modulation in the backward and forward coupled modes (Guo et al 2009).

6.3. Verification of Nonreciprocal Light Transmission

In order to prove the above-mentioned discussion, 2D finite-difference time-domain (FDTD) modelling is performed using Lumerical software package (Lumerical 2017). The electric vector of input electromagnetic waves was polarized in direction normal to the plane (TE mode was investigated).

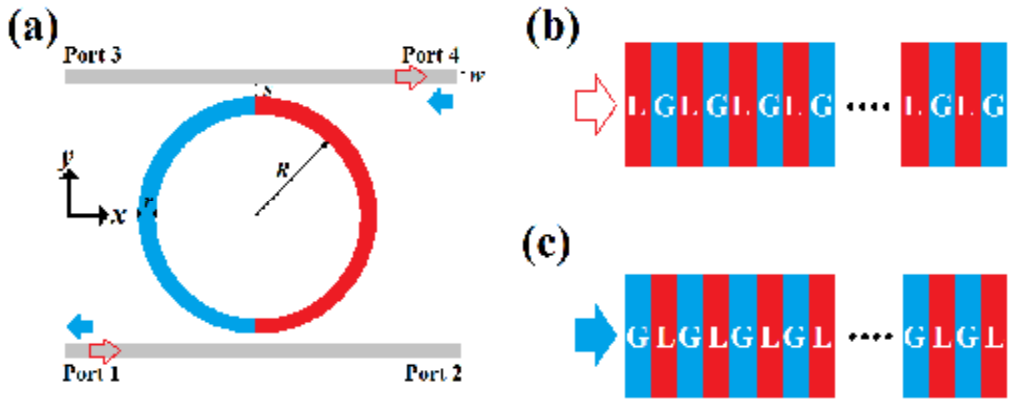

Figure 6.1. Designed add-drop ring resonator formed by gain-loss materials is schematically presented in (a). 1D PT symmetric structure that coupled light encounters while circulating the ring resonator in the cases of (b) forward (*From Port 1*) and (c) backward (*From Port 4*) incidences.

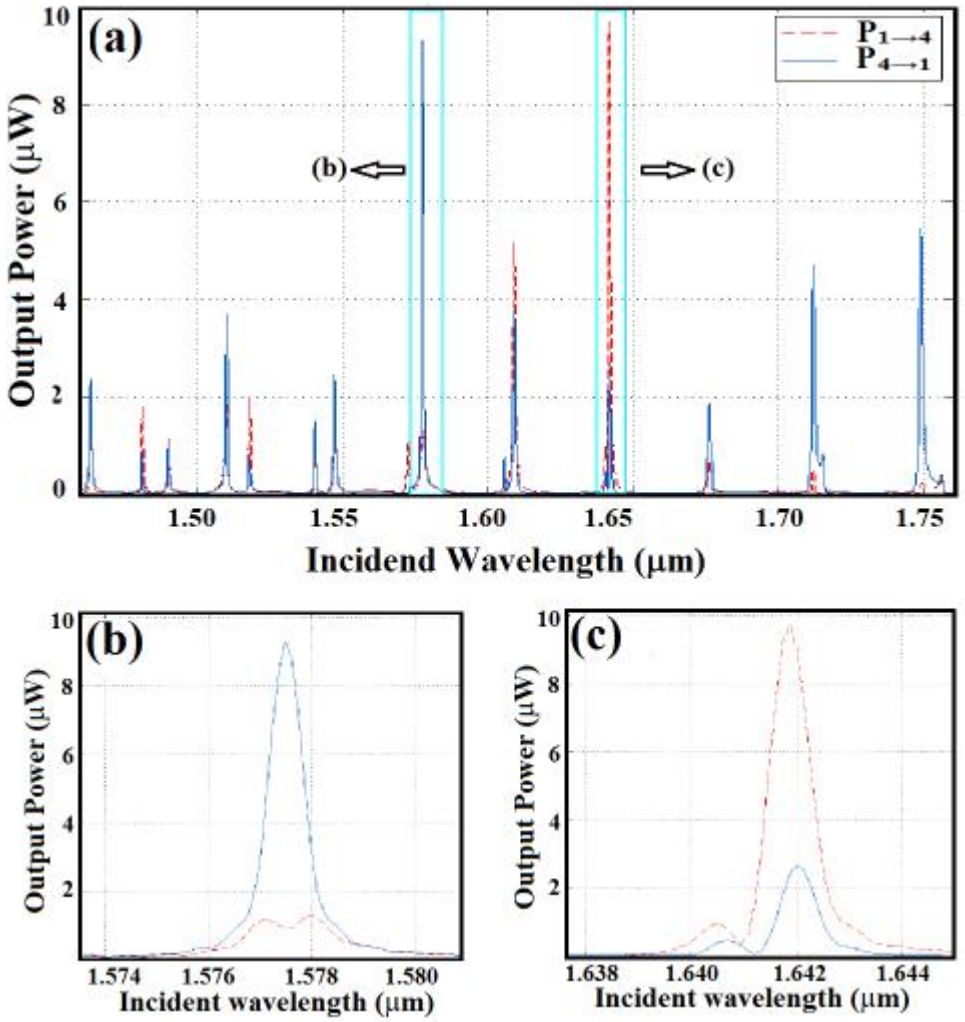

Figure 6.2. (a) Calculated output power spectra detected at Port 4 ($P_{1\to4}$) and Port 1 ($P_{4\to1}$). The output powera of two different resonant frequencies for (b) forward coupling at $\lambda = 1.577\,\mu m$ and (c) backward coupling at $\lambda = 1.642\,\mu m$.

The structure is illuminated by a broadband Gaussian pulse from Port 1 (Port 4) and the corresponding output power is monitored at Port 4 (Port 1), which we named as $P_{1\to4}$ ($P_{4\to1}$). The incident source with an average power of $3.70\,mW$ has a smaller width of $0.28\,\mu m$ than waveguide width in order to enhance beam

confinement. The calculated output power spectra for power incidence via Port 1 (forward) and Port 4 (backward) have been represented in Figure 6.2(a). The graph has been zoomed around two different resonant frequencies the Figures 6.2(b)-(c). As can be clearly seen from the figures 6.2(b)-(c), detected output powers are dependent on the left/right source illumination: at the resonant wavelength of $\lambda = 1.577\,mm$, the forward resonant mode ($P_{1\to4}$) is much more enhanced than backward one ($P_{4\to1}$) whereas at the operating wavelength of $\lambda = 1.642\,mm$, the resonant enhancement is inversed.

To better understand that condition, a term called power difference, ΔP, is defined having the following equation:

$$\Delta P = \frac{P_{1-4} - P_{4-1}}{\max(P_{1-4}, P_{4-1})} \tag{6.8}$$

The resulting power difference is plotted in Figure 6.3. That spectrum implies that the coupling mechanism in gain-loss balanced ring resonator varies depending on forward/backward incidence, which situation never happens in all-dielectric systems.

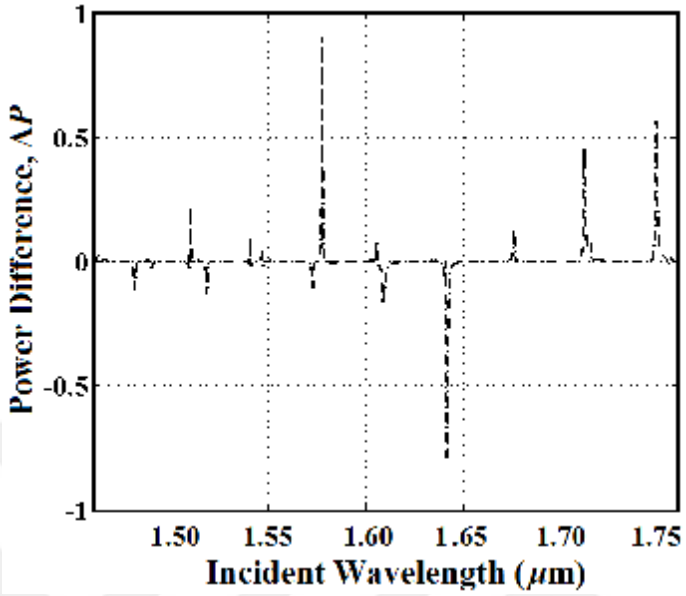

Figure 6.3. Normalized difference ΔP for the studied PT-symmetric configuration.

6.4. Conclusions

We propose a 2D add-drop ring resonator system that is composed of balanced gain-loss materials. The designed passive structure mimics a 1D PT-symmetric structure, due to showing different wave coupling mechanisms depending on the forward/backward light illumination (input channel), which are not observed in analogous all-dielectric configurations. Our discussion is numerically confirmed by 2D FDTD simulations. The calculated results show that our designs exhibit asymmetric resonant effects close to the resonance frequencies, suggesting that such types of microresonators could be applied in the field of asymmetric light propagation, for switching and sensing applications.

REFERENCES

Adamovsky, G., Wrbanek, S., 2013. Coupling of low-order LP modes propagating in cylindrical waveguides into whispering gallery modes in microspheres. Optics Express, 21: 2279-2286.

Agrawal, A., Sharma, A., 2004. Perfectly matched layer in numerical wave propagation: factors that affect its performance. Applied Optics, 43(21) 4225-4231.

Arfken, G. B., Weber, H. J., 2005. Mathematical Methods for Physicists, Elsevier Academic Press.

Armani, M., Kulkarni, R. P., Fraser, S. E., Flagan, R. C., Vahala, K. J., 2007. Label-Free, Single-Molecule Detection with Optical Microcavities, Science, 317:783-787.

Arnold, S., Comunale, J., Whitten, W., Ramsey, J., Fuller, K. A., 1992. Room-temperature microparticle-based persistent hole-burning spectroscopy, J. Opt. Soc. Am. B, 9(5): 819–824.

Bayer, M., Gutbrod, T., Reithmaier, J. P., Forchel, A., 1998. Optical Modes in Photonic Molecules. Phys. Rev. Lett., 81(12): 2582-2585.

Bender, C. M., 2007. Making sense of non-Hermitian Hamiltonians. Rep. Prog. Phys., 70: 947–1018.

Berenger, J. P., 1994. A perfectly matched layer for the absorption of electromagnetic waves. J. Comput. Phys, 114: 185–200.

Boettcher, S., Bender, C. M., 1998. Real spectra in non-Hermitian Hamiltonians having PT symmetry. Phys. Rev. Lett., 80(24): 5243-5246.

Boriskina, S. V., 2006. Theoretical prediction of a dramatic Q-factor enhancement and degeneracy removal of whispering gallery modes in symmetrical photonic molecules. Optics Letters, 31(3):338-340.

Boriskina, S. V., 2007. Spectral engineering of bends and branches in microdisk coupled-resonator optical waveguides. Opt. Express, 15(25):17371–17379.

Boriskina, S. V., 2010. Photonic Molecules and Spectral Engineering (I. Chremmos, O. Schwelb, N. Uzunoglu Editors). Photonic Microresonator Research and Applications, Springer, p. 393-422.

Chen, W. Y., Grover, R., Ibrahim, T. A., Van, V., Ho, P.-T., 2003. Compact singlemode benzocyclobutene microracetrack resonators. Integrated Photonics Research, Washington, DC.

Chen, Z., Taflove, A., Backman, V., 2004. Photonic nanojet enhancement of backscattering of light by nanoparticles: a potential novel visible-light ultramicroscopy technique. Optics Express, 12(7):1214-1220.

Chu, D. Y., Chin, M. K., Sauer, N. J., Xu, Z., Chang, T. Y., Ho, S. T., 1993. 1.5 μm InGaAs/InAlGaAs quantum-well microdisk lasers. IEEE Photonics Technology Letters, 5:1353–1355.

Connors, J. M. and Mahapatra, A., 1987. High finesse ring resonators made by silver ion exchange in glass. Journal of Lightwave Technology, LT-5(12):1686–1689.

Dadashi, Kh., Kurt, H., Ustun, K., Esen, R, 2014a. Graded Index Optical Microresonators: Analytical and Numerical Analyses, J. Opt. Soc. Am. B, 31: 2239–2245.

Dadashi, Kh., Turduev, M., Kurt, H., Esen, R., 2014b. Novel properties of Maxwell's fish eye as an optical microresonator. AES 2014 Symposium, Hangzhou, CHINA.

Djordjev, K., Choi, S. J., Dapkus, P. D., 2002. Microdisk Tunable Resonant Filters and Switches. IEEE Photonics Technology Letters, 14(6):828-830.

Falco, A. D., Kehr, S. C., Leonhardt, U., 2011. Luneburg lens in silicon photonics. Opt. Express, 19:5156-5162.

Feng, L., Wong, Z. J., Ma, R.-M., Wang, Y., Zhang, X., 2014. Single-mode laser by parity-time symmetry breaking. Science, 346(6212):972-975.

Franchimon, E. F., Hiremath, K. R., Stoffer, R., Hammer, M., 2013. Interaction of Whispering Gallery Modes in Integrated Optical Microring or Microdisk Circuits: hybrid coupled mode theory model. J. Opt. Soc. Am. B, 30(4):1048-1057.

Fuller, K. A., 1991. Optical resonances and two-sphere systems, Appl. Opt., 30:4716-4731.

Gabrielli L. H., Lipson, M., 2011. Integrated Luneburg lens via ultra-strong index gradient on silicon. Opt. Express 19:20122-20127.

Giden, I. H., Dadashi, Kh., Botey, M., Herrero, R., Staliuans, K., Kurt, H., 2015. Nonreciprocal light transmission in gain-loss modulated Micro ring resonators, presented at 17th. IEEE International Conference on Transparent Optical Networks (ICTON), Budapest, Hungary.

Giden, I. H., Dadashi, Kh., Botey, M., Herrero, R., Staliunas, K., & Kurt, H., 2016. Asymmetric Light Transmission in PT-Symmetric Microring Resonators. IEEE Journal of Selected Topics in Quantum Electronics, 22(5): 3600106.

Gopinath, A., Boriskina, S. V., Premasiri, W. R., Ziegler, L., Reinhard, B. M., Negro, L. D., 2009. Plasmonic Nanogalaxies: Multiscale Aperiodic Arrays for Surface-Enhanced Raman Sensing. Nano letters, 9(11):3922-3929.

Gomez-Reino, C., Perez, M. V., Bao, C., 2002. Gradient-Index Optics: Fundamentals and Applications. Springer.

Guo, A., Salamo, G. J., Duchesne, D., Morandotti, R., Volatier-Ravat, M., Aimez, V., Siviloglou, G. A., Christodoulides, D. N., 2009. Observation of PT-symmetry breaking in complex optical potentials. Phys. Rev. Lett., 103(9):093902(1-4).

Haavisto, J., Pajer, G. A., 1980. Resonance effects in low-loss ring waveguides. Optics Letters, 5:510–512.

Hara, Y., et al. 2005. Heavy photon states in photonic chains of resonantly coupled cavities with supermonodispersive microspheres. Phys. Rev. Lett., 94:203905.

Heebner, J., Grover, R., Ibrahim, T., 2008. Optical Microresonators Theory, Fabrication, and Applications. Springer, 263p.

Honda, K., Garmire, E. M., Wilson, K. E., 1984. Characteristics of an integrated optics ring resonator fabricated in glass. Journal of Lightwave Technology, LT-2:714–719.

Ishii, S., Babaa, T., 2005. Bistable lasing in twin microdisk photonic molecules, App. Phys. Lett., 87:181102.

Kurt, H., 2006. Photonic crystals: Analysis, design and biochemical sensing applications. Ph. D. thesis. Georgia Institute of Technology.

Leonhardt, U., 2009. Perfect imaging without negative refraction. New J. Phys., 11:093040-093051.

Leonhardt, U., Philbin, T. G., 2010. Perfect Imaging with Positive Refraction in Three Dimensions. Phys. Rev. A, 81:011804.

Li, Y., Abolmaali, F., Allen, K. W., Limberopoulos, N. I., Urbas, A., Rakovich, Y., Maslov, A. V., Astratov, V. N., 2017. Whispering gallery mode hybridization in photonic molecules. Laser Photonics Rev. 11(2):1600278(1-14).

Li, Y., Allen, K. W., Abolmaali, F., Maslov, A. V., Astratov1, V. N., 2014. Spectral Finger-Prints of Photonic Molecules. ICTON 2014, Tu.B6.6.

Lin, B. S., 2003. Variational analysis for photonic molecules: Application to photonic benzene waveguides. Phys. Rev. E, 68:036611.

Little, B. E., Chu, S. T., Haus, H. A., Foresi, J., Laine, J.-P., 1997. Microring resonator channel dropping filters, Jour. of Light. Tech. 15(6):998-1005.

Liu, J., Mendis, R., Mittleman, D. M., 2013. Mittleman, A Maxwell's Fish Eye Lens for the Terahertz Region. Appl. Phys. Lett., 103:031104(1-4).

Liu, S., Li, L., Lin, Z., Chen, H. Y., Zi, J., Chan, C. T., 2010. Graded index photonic hole: Analytical and rigorous full wave solution. Phys. Rev. B, 82(5):054204.

Lumerical FDTD Solutions, Inc. [online]. Availabe: https://www.lumerical.com, accessed on 2017.

Luneburg, R. K., 1964. Mathematical Theory of Optics. University of California Press.

Mahapatra, A., Robinson, W. C., 1985. Integrated-optic ring resonators made by proton exchange in lithium niobate, Applied Optics, 24:2285–2286.

Makowski, A. J., 2009. Exact, zero-energy, square-integrable solutions of a model related to the Maxwell's fish-eye problem. Annals of Physics, 324:2465–2472

Marcatili, E. A. J.,1969. Bends in optical dielectric guides. The Bell System Technical Journal, 48:2103–2132.

Miyazaki, H., Jimba, Y., 2000. Ab initio tight-binding description of morphology-dependent resonance in a biosphere. Phys. Rev. B, 62:7976.

Michler, P., Kiraz, A., Becher, C., Schoenfeld, W.V., Petroff, P.M., Zhang, L.,Hu, E., Imamoglu, A., 2000. A Quantum Dot Single-Photon Turnstile Device. Science, 290:2282-2285.

Möller, B. M., Woggon, U., Artemyev, M. V., 2007. Bloch modes and disorder phenomena in coupled resonator chains. Phys. Rev. B, 75: 245327(1-9).

Mukaiyama, T., Takeda, K., Miyazaki, H., Jimba, Y., Kuwata-Gonokami, M., 1999. Tight-Binding Photonic Molecule Modes of Resonant Bispheres, Phys. Rev. Lett., 82:4623.

Narimanov E. E., Kildishev, A. V., 2009. Optical black hole: Broadband omnidirectional light absorber. Appl. Phys. Lett. 95(4): 041106.

Oraevsky, A.N., 2002. Whispering-gallery waves, Quantum Electronics. 32(5) 377-400.

Oskooi, A. F., Roundy, D., Ibanescu, M., Bermel, P., Joannopoulos, J. D., Johnson, S. G., 2010. MEEP: A flexible free-software package for electromagnetic simulations by the FDTD method, Computer Physics Communications 181:687–702.

Peng, B., Özdemir, Ş. K., Lei, F., Monifi, F., Gianfreda, M., Long, G. L., Fan, S., Nori, F., Bender, C. M., Yang, L., 2014. Parity-time-symmetric whispering-gallery microcavities. Nat. Phys., 10(5):394–398.

Prkna, L., Ctyroky, J., Hubalek, M., 2004. Ring microresonator as a photonic structure with complex eigenfrequency. Opt. and Quan. Elect. 36:259-269.

Quan, H., Guo, Z., 2009. Analyses of whispering-gallery modes in small resonators. J. of Micro/Nanolithography, MEMS, and MOEMS, 8(3):033060.

Rabiei, P., Steier, W. H., Zhang, C., and Dalton, L. R., 2002. Polymer micro-ring filters and modulators. Journal of Lightwave Technology, 20,(11): 1968–1975.

Rafizadeh, D., Zhang, J. P., Hagness, S. C., Taflove, A., Stair, K. A., Ho, S. T., Tiberio, R. C., 1997. Waveguide-coupled AlGaAs/GaAs microcavity ring and disk resonators with high finesse and 21.6 nm free spectral range. Optics Letters, 22:1244–1246.

Rakovich Y. P., Donegan, J. F., 2010. Photonic atoms and molecules. Laser Photonics Rev, 4 (2):179–191.

Regensburger, A., Bersch, C., Miri, M.-A., Onishchukov, G., Christodoulides, D. N., Peschel, U., 2012. Parity-time synthetic photonic lattices. Nature, 488:167-171.

Rosu, H., Reyes, M., 1994. Electromagnetic Modes of Maxwell Fisheye Lens. IL Nuovo Cimento D 16:517-522.

Sandoghdar, V., Terussart, F., Hare, J., Lefevere-Seguin, V., Raimond, J.-M., Haroche, S., 1996. Very Low Threshold Whispering-Gallery-Mode Microsphere Laser. Phys. Rev. A, 54(3):1777-1780.

Schweiger, G., Horn, M., 2006. Effect of changes in size and index of refraction on the resonance wavelength of microspheres. J. Opt. Soc. Am. B, 23:212–217.

Shankar, R., 1994. Principles of Quantum Mechanics, Springer, New York.

Sheng, C., Liu, H., Wang, Y., Zhu, S. N., Genov, D. A., 2013. Trapping light by mimicking gravitational lensing. Nature Photonics, 7:902–906.

Shi, L., Tuzer, U., Xifré-Pérez, E., Fenollosa, R., García De Abajo F. J., Meseguer F., 2012. A New Photonic Atom: Submicron Silicon Nanocavities with Strong Magnetic Resonances in the Optical Region. ICTON 2012, Tu.C6.5.

Shopova, S. I., Zhou, H., Fan, X., Zhang, P., 2007. Optofluidic ring resonator based dye laser. Applied Physics Letters, 90:221101.

Stokes, L. F., Chodorow, M., Shaw, H. J., 1982. All-single-mode fiber resonator, Optics Letters. 7:288–290.

Sullivan, D. M., 2000. Electromagnetic Simulation Using the FDTD Method. IEEE Press.

Taflove, A., Brodwin, M. E. 1975. Numerical Solution of Steady- State Electromagnetic Scattering Problems Using the Time-Dependent Maxwell's equations. IEEE Transaction on Microwave Theory and Techniques, 23(8):623-630.

Taflove, A., Hagness, S. C. 2005. Computational Electrodynamics: The Finite-Difference Time-Domain Method. Artech House.

Tai, C. T., 1958. Maxwell Fish-eye treated by Maxwell Equations. Nature, 182: 1600-1601.

Tobing, L. Y.M., Dumon, P., 2010. Fundamental Principles of Operation and Notes on Fabrication of Photonic Microresonators (I. Chremmos, O. Schwelb, N. Uzunoglu Editors). Photonic Microresonator Research and Applications, Springer, p. 1-28.

Turduev, M., Botey, M., Giden, I. H., Herrero, R., Kurt, H., Ozbay, E., Staliunas, K., 2015. Two-dimensional complex parity-time-symmetric photonic structures. Phys. Rev. A, 91(2):023825(1-5).

Vahala, K. J., 2003. Optical Microcavities. Nature 424:839-846.

Walker, R. G. and Wilkinson, C. D. W., 1983. Integrated optical ring resonators made by silver ion-exchange in glass. Applied Optics, 22:1029–1035.

Wang, S., Ostrowski, M., YI, Y., 2011. Integrated Nano Photonic Molecule. ICTON 2011, Tu.A4.1.

Wang, Y., Sheng, C., Liu, H., Zheng, Y. J., ZHU, C., WANG, S. M., ZHU, S. N., 2012. Transformation bending device emulated by graded-index waveguide. Opt. Express, 20:13006-13013.

Weber, H. P., Ulrich, R., 1971. A thin-film ring laser. Applied Physics Letters, 19:38–40.

Wilk, T., Webster, S.C., Kuhn, A., Rempe, G., 2007. Single-Atom Single-Photon Quantum Interface. Science, 317:488-490.

Yariv, A., Xu, Y., Lee R. K., Scherer, A. 1999. Coupled-resonator optical waveguide: a proposal and analysis. Opt. Lett. 24(11):711–713.

Yee, K. S., 1966. Numerical Solution of Initial Boundary Value Problems Involving Maxwell's Equations in Isotropic Media. IEEE Transaction on Antennas and Propagation, 14:302-308.

Zentgraf, T., Liu, Y., Mikkelsen, M. H., Valentine, J., Zhang, X., 2011. Plasmonic Luneburg and Eaton lenses. Nature Nanotechnology, 6:151-155.

Zhu, D., Zhou, Y., Yu, X., Shum, P., Luan, F., 2012. Radially graded index whispering gallery mode resonator for penetration enhancement. Opt. Express, 20:26285-26291.

Zhu, J. G., Ozdemir, S. K., Xiao, Y. F., Li, L., He, L. N., Chen, D. R., 2010. On-chip single nanoparticle detection and sizing by mode splitting in an ultrahigh-Q microresonator. Nature Photonics, 4:46-49.

CURRICULUM VITAE

Khalil DADASHI received the B.Sc. degree in applied physics from the Isfahan University of Technology, Isfahan, Iran, in 1993, and the M.Sc. degree in solid state physics from the University of Tabriz, Tabriz, Iran, in 2008. Since 2011, he has been working toward the Ph.D. degree with Cukurova University, Adana, Turkey, and since 2012, he has been a Research Fellow with the Nanophotonic Research Group, TOBB University of Economics and Technology, Ankara, Turkey, working toward the Ph.D. degree. From 1995 to 2010, he was with the Research Institute for Applied Physics and Astronomy, University of Tabriz. His research interests include numerical analysis and design of photonic devices.